RESEARCH ARTICLE | MARCH 13 2024

# Mesoscale model for computational simulation of reaction driven by dielectric breakdown in metal-polymer propellants

Ju Hwan (Jay) Shin ● ; Min Zhou ✉ ●

View Online    Export Citation    CrossMark

# Mesoscale model for computational simulation of reaction driven by dielectric breakdown in metal-polymer propellants

Ju Hwan (Jay) Shin (ID) and Min Zhou[a] (ID)
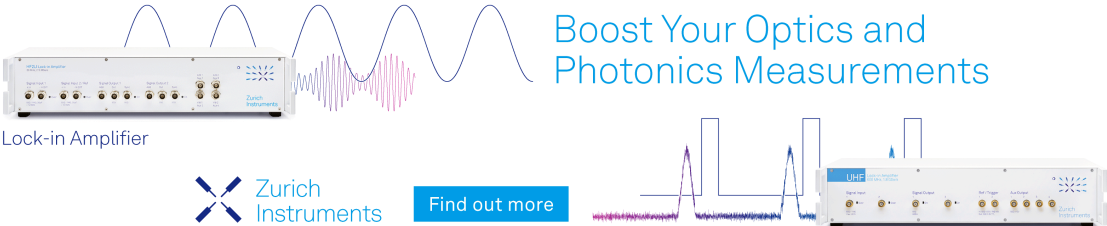
## AFFILIATIONS

The Woodruff School of Mechanical Engineering and the School of Materials Science and Engineering,
Georgia Institute of Technology, Atlanta, Georgia 30332, USA

[a] Author to whom correspondence should be addressed: min.zhou@gatech.edu; **Tel.:** 404-894-3294; **Fax:** 404-894-8336.

## ABSTRACT

The reactivity of heterogeneous energetic materials (HEMs) intimately depends on the underlying microstructural effects. For reactive materials, key factors include the microstructure distribution, morphology, size scale of heterogeneities, reactant mixing, and chemical kinetics of the reactants. We report the development of a mesoscale model for simulating the evolutions of the hotspot field and associated reaction processes when such materials are exposed to external excitations. The model explicitly accounts for microstructure, interdiffusion between the reactant species, advection of the species mixture, and chemical kinetics of the reaction. An Arrhenius relation is used to capture the rate of reactive heat release. The particular material analyzed is a composite of poly(vinylidene fluoride-co-trifluoroethylene) and nanoaluminum [or P(VDF-TrFE)/nAl]. The excitation leading to the initial microstructural temperature increase that kicks off the exothermic reactive processes is the dissipative heating arising from dielectric breakdown under the electric field developed through piezoelectricity and flexoelectricity of P(VDF-TrFE). As such, the model resolves both the breakdown process and the diffusion, advection, and exothermic reaction processes. The evolutions of the temperature and species distribution fields under the combined effects of breakdown and chemistry are used to predict the effects of microstructure, diffusion, and kinetics on several key metrics characterizing the reactive responses of the material. This mesoscale framework admits the quantification of uncertainties in these predicted macroscopic behavior measures due to microstructure heterogeneity fluctuations through the use of multiple, random but statistically equivalent microstructure instantiations. Although the particular hotspot inducing mechanism considered is dielectric breakdown here, the framework can be adapted to analyze reaction initiation and propagation and establish microstructure–reaction behavior relations under other types of hotspot inducing mechanisms, such as thermomechanical inelastic dissipation, frictional heating, and laser or microwave excitation.

## I. INTRODUCTION

Energetic materials (EMs) undergo chemical reactions in response to external stimulus and transition into combustion, explosion, or detonation over time scales spanning between femtoseconds and milliseconds.[1–3] The reactions in different EMs occur through different mechanisms. For instance, the reactions in polymer-bonded explosives (PBX) entail the self-decomposition of the energetic crystals.[4] For reactive materials (RMs) such as thermites, intermetallic compounds, and metal-polymer mixtures, the reactions require an intimate mixing of the reactants; therefore, various transport processes (e.g., diffusion and advection) are important,[5–12] in addition to

the chemical kinetic nature of the exothermic species. This was demonstrated by Lu *et al.*,[9] who developed a mesoscale simulation framework based on smoothed particle hydrodynamics (SPH) to quantify the ignition and energy release behavior of reactive materials. The heterogeneous nature of these materials dictates that microstructure (morphology, size scale, phase distribution, interfaces, and voids) plays an important role in their behavior.

To understand how reaction initiates and propagates in these materials, experimental observations and computational analyses at the microstructure level are necessary. Obviously, experiments at such small size scales and short time frames are challenging[13–15] and

often yielded limited information on the underlying mechanisms governing the reactivity of EMs. This is because many experimental observations are based on macroscopic measurements in which the effects of microstructure are averaged.[16] Experiments also cannot allow the behaviors of materials not yet available in the laboratory to be examined.[17] Computational simulations and analyses play an important role. Analyses require models that explicitly resolve the microstructure and track the relevant physical processes leading to the initiation and propagation of reactions.[18] For instance, Wei *et al.* developed a Lagrangian computational framework based on a meso-scale model for considering the combined thermomechanical and chemical heat dissipations and predicting the probabilistic ignition thresholds of heterogeneous energetic materials (HEMs).[17,19] Rai *et al.* also developed a framework for predicting the reaction behavior of octahydro-1,3,5,7-tetranitro-1,3,5,7-tetrazocine (or HMX) based on a mesoscale model in which the hotspot physics and thermo-chemistry are calculated in detail on nanosecond timescale, commensurate with the initiation of chemical reaction.[20] These models concern primarily chemical energy release through self-decomposition. While these studies have contributed to the understanding of reactivity of EMs, there is a lack of mesoscale models that allow the initiation and propagation of reactions in materials for which reactant mixing through transport mechanisms such as diffusion and advection plays a key role.

In this paper, we develop a mesoscale model for analyzing the evolution of the hotspot fields and associated reaction processes in a reactive material system. The model explicitly accounts for micro-structure, interdiffusion between the reactant species (individual movement of the reactants into each other), advection of the species mixture (bulk movement of the species mixture driven by the induced pressure gradient), and the chemical kinetics of the reaction. An Arrhenius relation is used to capture the rate of reactive heat release. The evolutions of temperature and species distributions under the combined effects of breakdown and chemistry are used to quantify the reactivity of the HEM. This mesoscale framework admits the quantification of uncertainties in the predicted behavior measures due to microstructure heterogeneity fluctuations through the use of multiple random but statistically equivalent microstructure instantiations.

The particular material analyzed is a composite of poly(vinyli-dene fluoride-co-trifluoroethylene) and nanoaluminum [or P(VDF-TrFE)/nAl]. The excitation leading to initial microstructural temperature rise that kicks off the exothermic reactive processes is due to the dissipative heating arising from dielectric breakdown under the localized electric field developed through piezoelectricity and flexoelectricity of P(VDF-TrFE). As such, the simulation resolves both the breakdown process and the interdiffusion, advec-tion, and exothermic reaction processes. Due to uncertainties in the knowledge of mesoscale material properties, several parametric studies are performed to determine the expected range of reactive behaviors under the same loading conditions. Specifically, the values for the diffusion coefficient and the chemical kinetics of the materials are parametrized within the ranges typically observed in experiments.[21–30] Although the particular hotspot inducing mecha-nism considered here is dielectric breakdown, the framework can be adapted to analyze the initiation and propagation of reaction and to establish microstructure–reaction relations under other

heating mechanisms, such as inelastic dissipation from mechanical deformation, frictional heating, and electromechanical and electro-magnetic excitations (e.g., laser, microwave heating). Consideration of the P(VDF-TrFE)/nAl system here is motivated by the growing interest in developing EMs that offer novel means of triggering and controlling the reaction. Despite concerted efforts to enhance the reliability and the tunability of EMs,[18,31–50] there remain challenges in the developments of EMs, due to gaps in our understanding of how various stimulus types (i.e., excitation) and microstructural designs influence their overall reactive behaviors at the macroscale.

Throughout this paper, the analysis framework for quantifying the reactivity of the HEMs is developed and discussed. The meso-scale analysis for capturing the development of the electric field (E-field) in the material under excitation that is responsible for the eventual initiation and growth of thermal hotspots within the micro-structure through heat-generating dielectric breakdown has been pre-viously detailed.[51,52] That analysis is only briefly outlined here and this paper accepts as input the E-fields obtained for different excita-tion conditions from the previous publications. The model resolves the dielectric breakdown and associated heat release, the spatial transport and temporal evolutions of the underlying reactant species based on an explicit consideration of the interdiffusion, advection, and chemical kinetics of the species. The resulting temperature and species distributions are used to systematically characterize the reac-tive behaviors of the material. Specific quantities of interest (QoI) include the ignition threshold or the minimum load intensity required for the initiation of self-sustaining, exothermic chemical reaction. Uncertainties in such QoI due to inherent randomness in the microstructure are also quantified.

As outlined in Fig. 1, the content of this paper is *Step 2* of a two-part series. *Step 1* concerns the development of the E-fields that kicks off the dielectric breakdown and reaction process, which has been fully discussed in previous publications.[52,53] The second part of the framework (*Step 2*), which is the focus of this paper, concerns the mesoscale model for computationally analyzing the
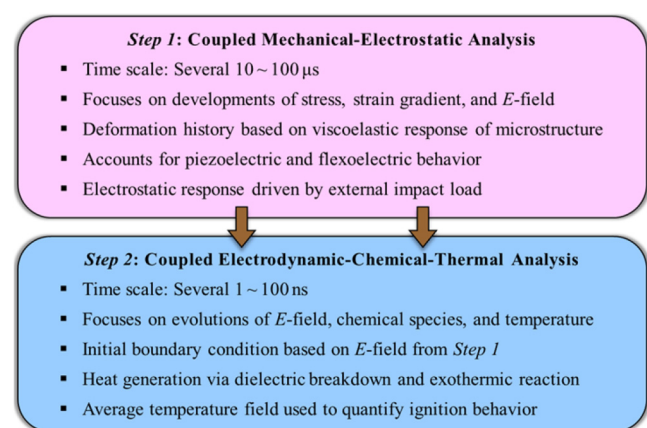


**FIG. 1.** Summary of the two-step sequential, mesoscale analyses framework developed for the systematic quantification of the reaction initiation and propaga-tion in P(VDF-TrFE)/nAl.

dielectric breakdown and initiation and growth of exothermic reactions in heterogeneous microstructures of reactive materials. The paper is organized as follows. In Sec. II, we provide an overview of the setup of the mesoscale computational framework developed. In Sec. III, we first state general features of the *E*-fields resulting from *Step 1*[52,53] that serve as the starting point of the analysis to come (Sec. III A), followed by a look at the process of reaction evolution in the heterogeneous microstructures (Sec. III B) and the determination of the reaction sensitivity of materials analyzed (Sec. III C). Section IV discusses the prediction of reactivity along with uncertainty quantification (UQ) through a probabilistic analysis. In Sec. V, the effects on overall reaction sensitivity of different microstructure attributes, such as particle size, particle volume fraction, particle dispersity, porosity, and void size, are analyzed. Finally, we summarize primary points of the findings in Sec. VI.

## II. FRAMEWORK OF ANALYSIS

The overall framework is designed to capture the entire processes of excitation-induced field development, hotspot generation, transport, initiation and growth of reaction, and transition of species from condensed phase to gaseous phase. For the material system of P(VDF-TrFE)/nAl, the excitation is mechanical impact loading, where the energy imparted into the material leading to

hotspot development is in the form of *E*-field generated through mesoscale piezoelectric and flexoelectric effects and the initial hotspot field that kicks off the transport and reaction processes is due to dielectric breakdown caused by high *E*-field. A two-step, sequential analyses framework is developed. As illustrated in Fig. 1, the first part of the analyses (*Step 1*), as detailed previously,[51,52] focuses on the development of electric field within the material as a function of time and applied loading. In *Step 2*, which is the focus of this paper, the electrical fields from *Step 1* are used as part of the input and initial condition for the analysis of hotspot generation through dielectric breakdown, transport, exothermic reaction initiation and propagation, and transition of species from condensed phase to gaseous phase. This two-step framework is necessary, as the dominant physical processes and the time scales of the two stages of events are vastly different (Fig. 1).

The mesoscale computational framework focuses on the effects of microstructure, transport, and chemical kinetics on the overall reaction process. Characterization of the reactive behavior uses the evolutions of the temperature and species fields resulting from the simultaneous account of dielectric breakdown and exothermic reaction processes. In particular, the overall time to ignition and ignition threshold (minimum input energy required for ignition) is predicted, along with uncertainty quantification as illustrated in Fig. 2.
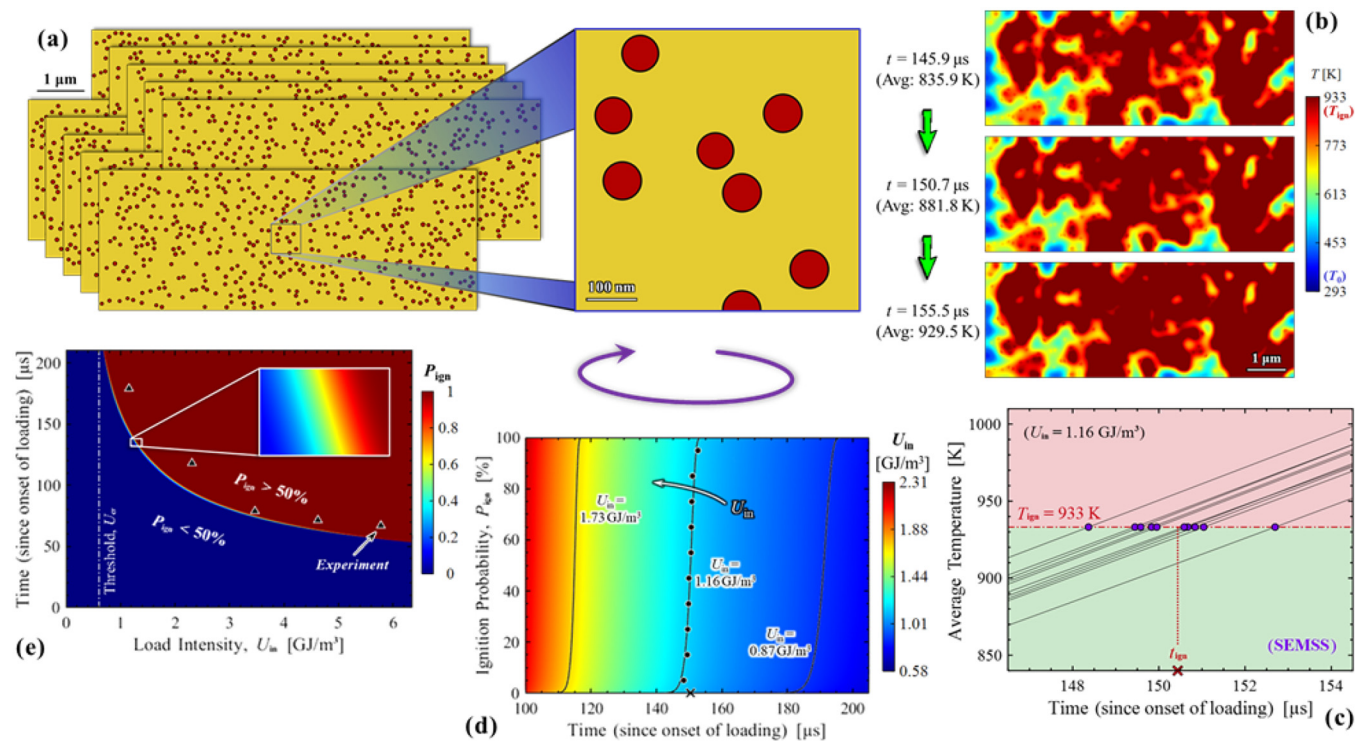


**FIG. 2.** Mesoscale framework for explicit analyses of reaction initiation and growth and prediction of macroscopic reaction behavior with uncertainty quantification (UQ). (a) Generation of microstructure instantiations; (b) hotspot formation due to external excitation; (c) determination of the onset of ignition; (d) and (e) prediction of the macroscopic behavior and behavior measures with UQ.

Local breakdown occurs when the $E$-field intensity at a material location exceeds the material's breakdown strength and leads to the dissipation of heat through the associated phase transition. This initial rise in temperature facilitates the interdiffusion process and results in the mixing of the reacting species. Once the local temperature of the mixture exceeds a certain value (the ignition temperature, or $T_{ign}$), chemical reaction is subsequently triggered among the reactant species. For P(VDF-TrFE)/nAl, the two reactants are aluminum and PVDF.[54–61] The reaction also leads to significant energy release in the form of dissipative heat, due to its exothermicity. The reaction rate correlates with the overall magnitude of the temperature distribution,[62] as it is dependent on the ratio of the energy acquired by the material to the activation energy ($e_a$). As a result, the material experiences spiraling cycles of rapid temperature rise, owing to the catalytic effects of heating on reaction rate and vice versa. As long as the rate of heat dissipation via chemistry surpasses the rate of heat loss through thermal conduction, the material sustains its reaction locally. This self-sustaining, exothermic reaction progresses until one of the reactant species is fully consumed.
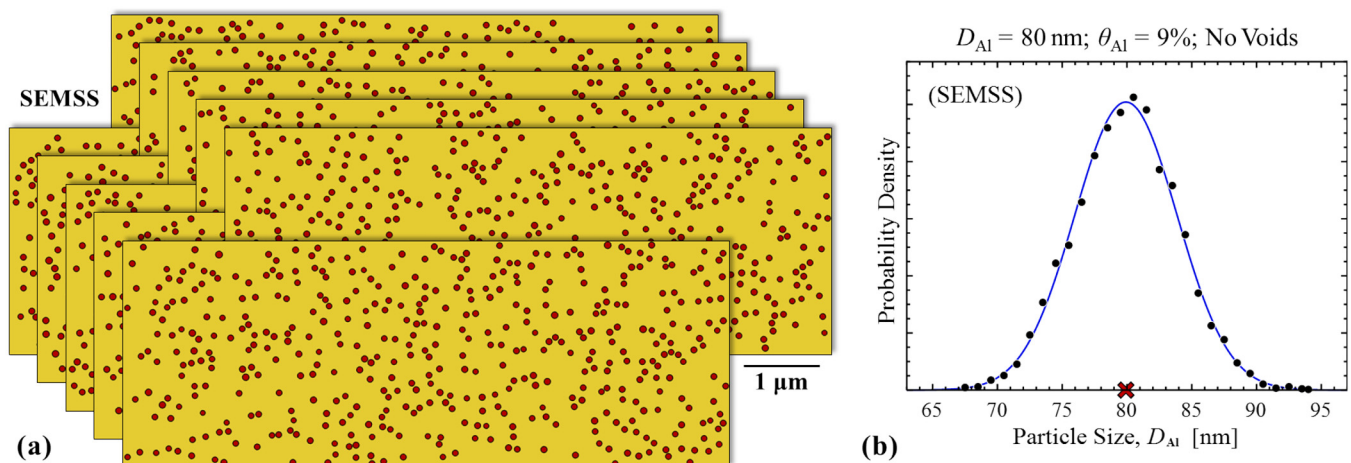
## A. Microstructure generation

The computational model explicitly resolves the heterogeneous microstructure of the material. Microstructure generation captures the overall statistical attributes of the material used in the experiment.[53] As shown in Fig. 3, the microstructure model is $8 \times 3 \ \mu m^2$ in size and comprises nAl particles embedded within the P(VDF-TrFE) polymer with a volume fraction of $\theta_{Al} = 9\%$. The particles are circular core–shell structures with a mean outer diameter ($D_{Al}$) of 80 nm[63] and a standard deviation of 4 nm. The inner Al core has a mean radius of 36.7 nm, while the outer $Al_2O_3$ shell (aluminum oxide) has a thickness of 3.3 nm, consistent with the samples used in the experiments.

The finite element discretization uses isoparametric, first-order, Lagrange, mostly triangular elements with an average element size of ~8 nm. For the set of microstructures shown in Fig. 3(a), the number of elements in each microstructure is ~575 000. To capture the microstructural effects responsible for the stochastic variations in the reactive behavior, a statistically equivalent microstructure sample set (SEMSS) consisting of ten random but statistically similar specimens is generated for each material setting. This approach of using multiple instantiations of random samples has been employed in many publications concerning several material systems, including ceramic composites,[64–66] polymer-bonded explosives,[19,67,68] metals,[69,70] and metal-polymer propellants.[52,71,72] The number of microstructure instantiations in sample each set ranged from 50, 20, 10 to 5. Together, these papers showed that the results may differ depending on how the multiple instantiations differ from each other statistically. In many cases, the outcome is similar when 5, 10, or 20 instantiations are used. One key aspect is how the microstructure morphology varies from sample to sample. In this paper, all particles have the same shape (i.e., circular) and the difference is only in the spatial distribution. Therefore, ten instantiations capture most of the variations.

Using Intel Xeon Gold 6226 cluster (two sockets with one core), the simulation of electromechanical response under impact (*Step 1*) took ~6 single-processor minutes, while the simulation of dielectric breakdown and exothermic reaction (*Step 2*) took ~65 single-processor hours. The computational setup for the two aforementioned simulations will be outlined in detail later in the paper.

Furthermore, a total of 12 SEMSSs are generated (not all shown here for brevity), each with ten random microstructure instantiations. These SEMSSs concern ranges of mean particle size ($D_{Al} = 70–85$ nm), particle volume fraction ($\theta_{Al} = 7\%–11\%$), particle dispersity index ($\xi_{Al} = 0.65–1.49$), mean void size ($D_{vd} = 100–200$ nm), and void volume fraction ($\theta_{vd} = 5\%–10\%$). Both $D_{Al}$ and $D_{vd}$ vary based on a Gaussian distribution, similar to that



**FIG. 3.** (a) A statistically equivalent microstructure sample set (SEMSS) comprising ten randomly generated specimens; (b) probability density function of the Al particle size (diameter) distribution.
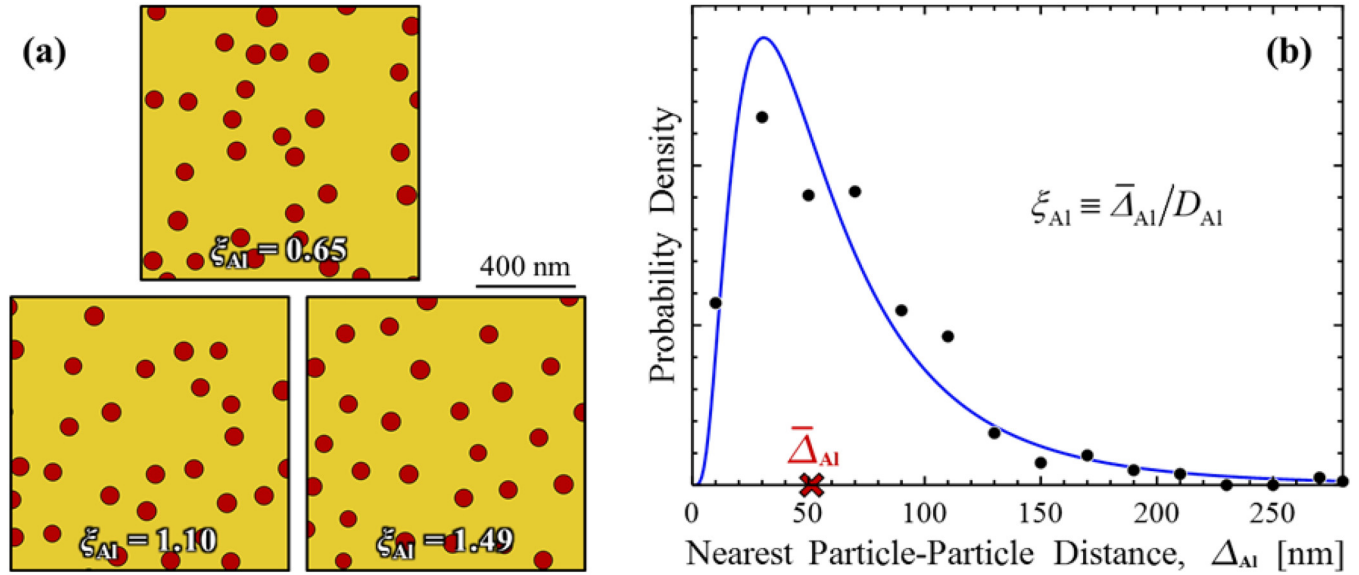
**FIG. 4.** (a) Inset views of microstructures with a mean particle size of 80 nm and an dispersity index varying between 0.65 and 1.49; (b) probability density function of nearest particle–particle distance and characterization using a lognormal distribution.

shown in Fig. 3(b). The particle dispersity index represents the ratio $\xi_{Al} \equiv \bar{\Delta}_{Al}/D_{Al}$, where $\bar{\Delta}_{Al}$ is the median nearest particle–particle distance, and is illustrated in Fig. 4. In this paper, the set of microstructures whose attributes are consistent with those tested in the accompanying experiment[53] is referred to as the *baseline* configuration ($D_{Al} = 80$ nm, $\theta_{Al} = 9\%$, $\xi_{Al} = 0.65$, and no voids). The other SEMSSs are variations based on the baseline case and are used to explore the effects of microstructure variations on the material behavior. Most of the analysis results delineated herein are shown for the baseline case.

It is noted that the oxide layers ($Al_2O_3$) on the individual Al particles are not explicitly modeled when it comes to the chemistry modeling in *Step 2* of the analyses, although they are explicitly considered in all other accompanying analyses in *Step 1*. One reason is due to the lack of detailed reaction and diffusion models involving Al, $Al_2O_3$, and the polymer. Instead, the parametric studies carried out here by varying the kinetic properties (e.g., diffusion coefficients and reaction rate constant) can be considered a form of implicit exploration of the effect in a phenomenological manner. The parameters chosen are within the ranges typically reported from experiments.[22,28–30] A detailed treatment of the oxide layers and reaction kinetics may be considered in the future.

### B. Governing equations

For the materials and conditions of interest, the effect of induction (i.e., magnetism) is negligible; the electrodynamic response of the materials during dielectric breakdown is governed by Faraday's and Ampère's laws in the form of

$$\begin{cases} \nabla \times \boldsymbol{E} = \boldsymbol{0}, \\ \nabla \cdot \boldsymbol{J} = -\partial \rho_q/\partial t, \end{cases} \tag{1}$$

where $\boldsymbol{J}$ is the total electric current density comprising both the free and bound current terms.

The transport of the species is governed by the conservations of mass, momentum, and species, i.e.,

$$\begin{cases} \dfrac{\partial \rho}{\partial t} + \nabla \cdot (\rho \dot{\boldsymbol{u}}) = 0, \\ \rho \dfrac{\partial \dot{\boldsymbol{u}}}{\partial t} + \rho(\dot{\boldsymbol{u}} \cdot \nabla)\dot{\boldsymbol{u}} = -\nabla p + \nabla \cdot \boldsymbol{\tau}_{\text{dev}}, \text{ and} \\ \rho \dfrac{\partial \omega_{(n)}}{\partial t} + \rho(\dot{\boldsymbol{u}} \cdot \nabla)\omega_{(n)} + \nabla \cdot \boldsymbol{j}_{(n)} = \Lambda_{(n)}, \end{cases} \tag{2}$$

where $\rho$, $\dot{\boldsymbol{u}}$, and $\omega_{(n)}$ denote the mass density, mass-averaged velocity, and mass fraction of the $n$th species, respectively; $\boldsymbol{j}_{(n)}$ and $\Lambda_{(n)}$ are the mass flux of the $n$th species relative to $\dot{\boldsymbol{u}}$ and the production (or consumption) rate of the $n$th species, respectively; $p$ and $\boldsymbol{\tau}_{\text{dev}}$ are the absolute pressure and the deviatoric part of the Cauchy stress, respectively.

The transient thermal response is governed by the conservation of energy as

$$\rho c_p \frac{\partial T}{\partial t} = \kappa \nabla^2 T + \sigma |\boldsymbol{E}|^2 + r\Delta H, \tag{3}$$

where $c_p$, $T$, $\kappa$, and $\sigma$ denote the specific heat at constant pressure, local temperature, isotropic thermal conductivity, and electrical conductivity, respectively (see Table I). In the simulations, temperature-dependency of the material properties is assumed wherever appropriate, including the mass density, specific heat, and thermal conductivity of the P(VDF-TrFE) binder, which are obtained from Ref. 73 and of the nAl particles, which are obtained

**TABLE I.** Electrodynamic and thermal properties at room temperature.[73–75]

| Material | $\sigma_0$ (S/m) | $\sigma_{bd}$ (S/m) | $\rho$ (kg/m$^3$) | $c_p$ [J/(kg K)] | $\kappa$ [W/(m K)] |
|---|---|---|---|---|---|
| P(VDF-TrFE) | $7 \times 10^{-12}$ | 1 | 1938 | 1172 | 0.181 |
| Aluminum | $3.77 \times 10^7$ | ... | 2702 | 930 | 165 |
| Al$_2$O$_3$ | $10^{-12}$ | ... | 3960 | 740 | 47.8 |

from Ref. 74. The two heat-source terms on the right-hand side of the equation represent the electrical dissipation caused by the dielectric breakdown and the chemical dissipation caused by the enthalpy of reaction, respectively. The enthalpy of reaction ($\Delta H$) leading to the ignition of P(VDF-TrFE)/nAl is 55 MJ/kg.[51]

In the modeling of the dielectric breakdown, the constitutive relation for the total current density is

$$J_i = \sigma E_i + \partial D_i/\partial t, \tag{4}$$

where the terms on the right-hand side of the equation represent the conduction current density induced by the local electric field and the displacement current density, respectively. Fourier's law is used to calculate the heat flux density ($\dot{\boldsymbol{Q}}$) via

$$\dot{\boldsymbol{Q}} = -\kappa \nabla T. \tag{5}$$

In the species transport equations, the constitutive relation based on Fick's law for the mass flux of the $n$th species is

$$\boldsymbol{j}_{(n)} = -\rho f_{(n)}(\nabla \omega_{(n)} + \omega_{(n)} \nabla M/M) + \rho \omega_{(n)} \sum_{n=1}^{\psi} f_{(n)} \frac{M_{(n)}}{M} \nabla \chi_{(n)}, \tag{6}$$

where $f_{(n)}$ denotes the isotropic diffusion coefficient (see Table II); $M_{(n)}$ and $M$ are the molar mass of the $n^{th}$ species and the mean molar mass of the mixture, respectively; $\chi_{(n)}$ is the mole fraction of the $n^{th}$ species; $\psi$ represents the total number of species present.

The rate of production (or consumption) of $n$th species is given as

$$\Lambda_{(n)} = \zeta_{(n)} M_{(n)} k \prod_{n \, \in \, \text{reac}} \left( \frac{\rho \omega_{(n)}}{M_{(n)}} \right)^{-\zeta_{(n)}}, \tag{7}$$

where $\zeta_{(n)}$ is the stoichiometric coefficient of the $n$th species. Here, $k$ denotes the rate constant, whose formulation is based on the

**TABLE II.** Transport properties at room temperature.

| Material | $f$ (m$^2$/s) | $\eta$ (Pa s) |
|---|---|---|
| Al | $10^{-9}$ | $10^2$ |
| PVDF | $10^{-9}$ | $10^2$ |
| Prod$_{(g)}$ | $10^{-5}$ | $10^{-4}$ |

temperature-dependent Arrhenius equation of the form

$$k(T) = A \exp\left(\frac{-e_a}{R_g T}\right), \tag{8}$$

where $A$, $e_a$, and $R_g$ represent the frequency factor ($A = 7.524 \times 10^{10} \text{ s}^{-1}$), the activation energy ($e_a = 62.7$ kJ/mol), and the universal gas constant which is 8.314 J/(mol K), respectively.[22]

It is assumed that the constitutive relation for the deviatoric part of the Cauchy stress [as shown in the Navier–Stokes equation in Eq. (2)] follows that of a Newtonian fluid for which

$$\boldsymbol{\tau}_{\text{dev}} = \eta \left[ \nabla \dot{\boldsymbol{u}} + (\nabla \dot{\boldsymbol{u}})^{\text{T}} - \frac{2}{3}(\nabla \cdot \dot{\boldsymbol{u}})\boldsymbol{I} \right], \tag{9}$$

where $\eta$ is the dynamic viscosity. $\boldsymbol{\tau}_{\text{dev}}$ is the difference between the total Cauchy stress ($\boldsymbol{\tau}$) and the hydrostatic stress tensor of $\frac{1}{3}\text{tr}(\boldsymbol{\tau})\boldsymbol{I}$.

To account for the latent heat of fusion associated with the endothermic melting from solid to liquid, the phase transformation of the materials is explicitly considered in the thermal analysis of the simulation. This transition occurs at a melting temperature ($T_{\text{m}}$) of 425 K for PVDF[73] and 933 K for Al[74,75] and is modeled using the apparent specific heat in the form of

$$c_p(\phi, T) = \phi c_{p1} + (1 - \phi)c_{p2} + L\frac{\partial \pi_{\text{m}}}{\partial T}, \tag{10}$$

which accounts for the energy absorption due to latent heat. Here, $c_{p1}$ and $c_{p2}$ denote the specific heat capacities of the solid and molten states at constant pressure, respectively; $\phi$ and $L$ are the volume fractions of the solid phase and the latent heat, respectively; $\pi_{\text{m}}$ is defined as $\pi_{\text{m}} \equiv 0.5 - \phi$.
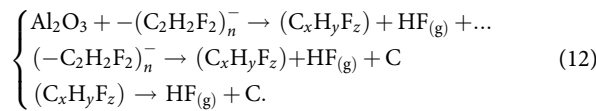
Dielectric breakdown is explicitly modeled[71] in the polymer binder using a conditional function of the form

$$\sigma(\boldsymbol{x}, t) = \begin{cases} \sigma_0, & \text{if } \max_{t \in [t_{\text{bd}}, t]} |\boldsymbol{E}(\boldsymbol{x}, t)| < E_{\text{bd}} \\ \sigma_{\text{bd}}, & \text{if } \max_{t \in [t_{\text{bd}}, t]} |\boldsymbol{E}(\boldsymbol{x}, t)| \geq E_{\text{bd}} \end{cases}, \tag{11}$$

where $\sigma$ denotes the local electrical conductivity; $\sigma_0$ is the initial conductivity prior to breakdown (see Table I); $t_{\text{bd}}$ is the specified time of breakdown initiation; $\sigma_{\text{bd}}$ is the post-breakdown conductivity ($\sigma_{\text{bd}} \gg \sigma_0$); and $E_{\text{bd}}$ is the dielectric breakdown strength. This piecewise function states that the electrical conductivity at a material point changes irreversibly to a higher value (i.e., $\sigma_{\text{bd}}$) once the local $E$-field exceeds the breakdown strength.

The set of chemical reactions leading to the initiation and growth of the exothermic reaction for P(VDF-TrFE)/nAl[54] are summarized in Eq. (12). Here, the first reaction describes the decomposition of PVDF [i.e., $(C_2H_2F_2)_n$], while the second and third reactions, which occur simultaneously, pertain to the direct pyrolysis of PVDF and the decomposition of the intermediate

14 March 2024 04:23:33

species (i.e., $C_xH_yF_z$), respectively,

$$\begin{cases} Al_2O_3 + -(C_2H_2F_2)_n^- \rightarrow (C_xH_yF_z) + HF_{(g)} + \ldots \\ (-C_2H_2F_2)_n^- \rightarrow (C_xH_yF_z) + HF_{(g)} + C \\ (C_xH_yF_z) \rightarrow HF_{(g)} + C. \end{cases} \quad (12)$$

The chemical reactions listed above represent the kinetic processes culminating in the production of gaseous hydrogen fluoride (HF). Subsequently, these newly created HF molecules react with Al atoms (i.e., fluorination) to form aluminum fluoride ($AlF_3$), which can be stated as

$$2Al + 6HF_{(g)} \rightarrow 2AlF_3 + 3H_{2(g)}. \quad (13)$$
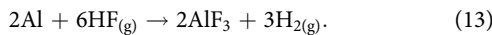
For the present analysis, the predominant mechanism responsible for the initiation of exothermic reaction within the material is identified and captured. Since the fluorination step represents the most exothermic process in the set of reactions delineated in Eqs. (12) and (13), the multi-stage reaction is simplified and combined into a single-stage, forward kinetic reaction model in the form of

$$Al + PVDF \rightarrow prod_{(g)}. \quad (14)$$
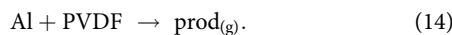
Recognizing that the mass density of a gaseous mixture varies according to its appropriate equation of state (EOS) that is distinct from that of its condensed phase (i.e., solid and liquid), the density is modified into a piecewise smooth function to account for this dual behavior through

$$\rho(\boldsymbol{x}, t) = \begin{cases} \sum_{n=1}^{\psi} \omega_{(n)} \rho_{(n)}(T), & T < T_m \\ p/R_g T, & T \geq T_m \end{cases}. \quad (15)$$

In Eq. (15), the density of the condensed phase (prior to melting) is a function of temperature only and is computed based on the rule of mixture. The density of the gaseous phase (after melting) is computed based on the ideal gas law and varies based on both pressure and temperature. More realistic EOS can be used if the information is made available in the future.

## III. INITIATION AND PROPAGATION OF CRITICAL HOTSPOTS IN MICROSTRUCTURE

### A. Development of electric field under impact (Step 1)

The starting point of the current analysis is the state of the material at which an $E$-field of sufficient magnitude is developed via analysis in *Step 1*, as previously reported.[52] One example is shown in Fig. 5, where the interfacial regions along the Al particles are seen to have a localized intensification of the $E$-field. Here, the induced electrical response of the P(VDF-TrFE)/nAl is due to the combination of piezoelectric and flexoelectric properties of the polymer binder. The excitation is applied to the composite specimen in the form of external impact loading whose intensity is characterized using the initial input energy per unit volume (i.e., $U_{in} = mgh_0/V_{\Omega}$, where $mgh_0$ represents the kinetic energy delivered to the specimen at the
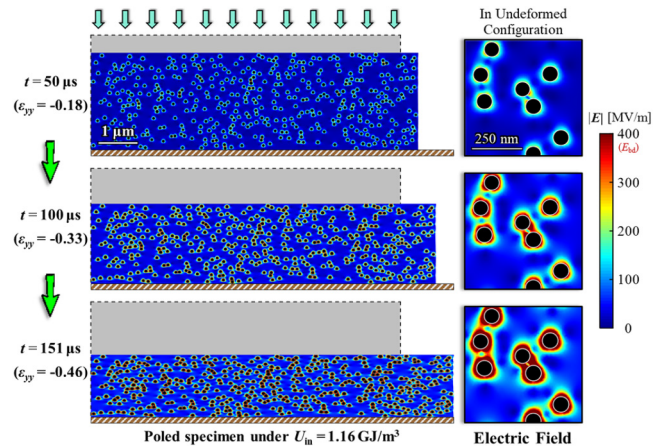


**FIG. 5.** Evolution of $E$-field distribution for one of the microstructures shown in Fig. 3(a). The load intensity is $U_{in} = 1.16 \, GJ/m^3$.

onset of impact with a drop height of $h_0$; $V_{\Omega}$ is the total volume of the undeformed specimen).

Once the local $E$-field magnitude exceeds the local breakdown strength ($E_{bd}$) of the P(VDF-TrFE) binder, dielectric breakdown initiates. This occurs primarily in the interfacial regions between the particles and the P(VDF-TrFE) binder where the $E$-field is the highest, resulting in the sudden loss of the material's ability to withstand the high electrical load as well as the local transition into a conductive phase. For the microstructures and the range of load intensities considered, it is shown that the heat generated via resistive current (also known as Joule heating) serves as the initial dissipation responsible for kicking off the onset of chemistry and ultimately the self-sustaining, exothermic reaction.

In Fig. 6, inset views of the local $E$-field magnitude are shown around the Al particles and voids. For the loading conditions considered ($t = 150 \, \mu s$ and $U_{in} = 1.16 \, GJ/m^3$), Fig. 6 shows that the microstructural heterogeneities, such as Al particles and voids, can substantially enhance the overall local $E$-field intensities beyond the breakdown strength of the polymer binder.

### B. Electrodynamic–chemical–thermal analysis (Step 2)

To examine the total heat dissipated via dielectric breakdown and exothermic reaction, a multiphysics simulation framework is developed. Here, the electric potential distribution (or alternatively the $E$-field) from the coupled mechanical-electrostatic analysis (*Step 1*) is used as part of the initial conditions for the electrodynamic–chemical–thermal analysis (*Step 2*). The evolutions of the temperature field, the species, and pressure within the material undergoing dielectric breakdown and exothermic reaction are tracked.

Dielectric breakdown is modeled in the P(VDF-TrFE) binder alone, as the Al core of the particles is electrically conductive and the aluminum oxide ($Al_2O_3$) shell has a substantially high breakdown strength, precluding the initiation of breakdown in the $Al_2O_3$ under the conditions analyzed. The energy dissipated during the
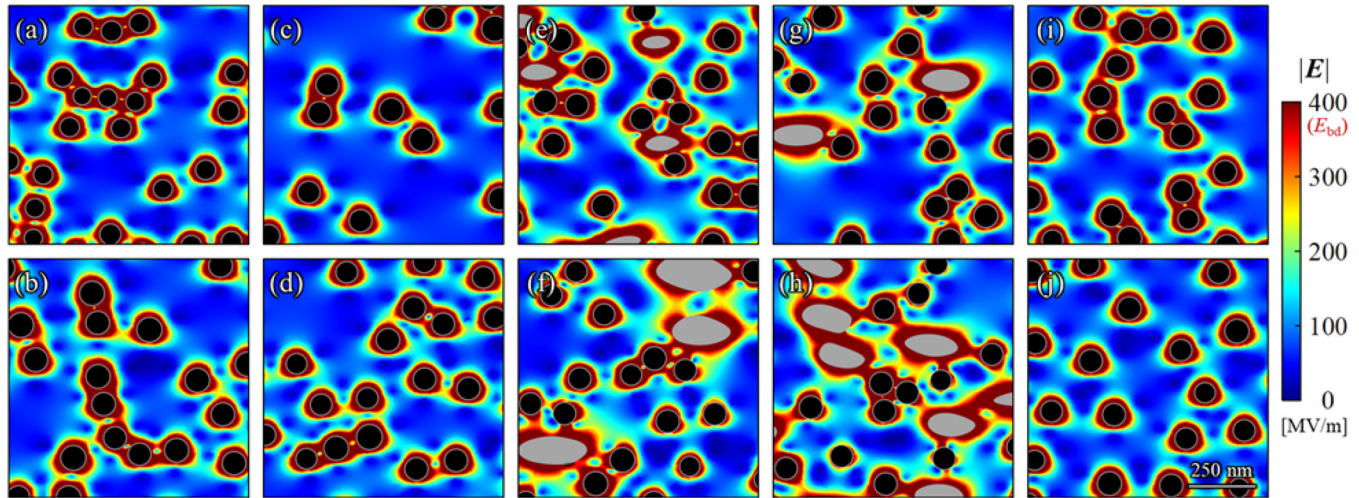
**FIG. 6.** (a) Inset views of local $E$-field around particles (black) and voids (gray). (a) $D_{Al} = 70$ nm, $\theta_{Al} = 9\%$, no voids; (b) $D_{Al} = 85$ nm, $\theta_{Al} = 9\%$, no voids; (c) $D_{Al} = 80$ nm, $\theta_{Al} = 7\%$, no voids; (d) $D_{Al} = 80$ nm, $\theta_{Al} = 11\%$, no voids; (e) $D_{Al} = 80$ nm, $\theta_{Al} = 9\%$, $D_{vd} = 100$ nm, $\theta_{vd} = 5\%$; (f) $D_{Al} = 80$ nm, $\theta_{Al} = 9\%$, $D_{vd} = 200$ nm, $\theta_{vd} = 5\%$; (g) $D_{Al} = 80$ nm, $\theta_{Al} = 9\%$, $D_{vd} = 150$ nm, $\theta_{vd} = 5\%$; (h) $D_{Al} = 80$ nm, $\theta_{Al} = 9\%$, $D_{vd} = 150$ nm, $\theta_{vd} = 10\%$; (i) $D_{Al} = 80$ nm, $\theta_{Al} = 9\%$, $\xi_{Al} = 0.65$, no voids; (j) $D_{Al} = 80$ nm, $\theta_{Al} = 9\%$, $\xi_{Al} = 1.49$, no voids. All cases are shown in the deformed configuration and for $t = 150$ μs with $U_{in} = 1.16$ GJ/m³.

breakdown process leads to local temperature rise via resistive heating. The heat release via the dielectric breakdown facilitates the interdiffusion and advection processes of the underlying chemical species (i.e., Al, PVDF, and product), leading to even higher temperature rise due to the exothermic reaction between the reactants. The electrical and chemical dissipations continue to progress until their respective prerequisites for heating (e.g., $E$-field intensity and the remaining concentrations of the reactant species) are fully consumed.

## C. Simulation results

The evolutions of the $E$-field, Al mass fraction, and temperature distributions are shown in Fig. 7 for the baseline microstructure undergoing dielectric breakdown and exothermic reaction. Here, the breakdown initiates at 151 μs after the application of mechanical excitation (at a load intensity of $U_{in} = 1.16$ GJ/m³). The initial $E$-field magnitude is at its peak level at the onset of breakdown and is directly obtained from the previous mechanical–electrostatic analysis (*Step 1*). After breakdown begins, the local $E$-field intensity attenuates rapidly at first and slows as the intensity reduces.

As illustrated in Fig. 8, the overall Al and PVDF mass fractions in the microstructure also decrease over time ($\sim 10^2$ ns). This evolution in chemical species concentration is due to interdiffusion (i.e., local transport of the Al and PVDF species, leading to the consumption of the reactant species and the production of the gaseous product species) and advection (i.e., bulk transport of the species mixture as a result of the induced pressure gradient within the microstructure). Owing to the highly localized $E$-field intensity as well as the presence of both reactant species necessary for chemical reaction, the temperature initially increases near the particle–binder

interfaces. The elevated temperature subsequently permeates throughout the rest of the microstructure, due to thermal conduction and convection.

In Fig. 9, the time histories of the species mass fractions and temperature are shown for the baseline microstructure and loading conditions discussed in Figs. 7 and 8. Here, the average value for the microstructure is calculated and plotted. For the reactant species (i.e., Al and PVDF), the mass fractions are normalized by their respective initial value at $t = t_{bd}$. It can be seen that the species concentrations and temperature all tend toward a steady-state value eventually. The average mass fractions of both Al and PVDF decrease monotonically, while that of the product species and the average temperature increase. Over time, the average Al mass fraction (denoted as [Al]) approaches zero, while [PVDF] and [prod] converge to a non-zero, finite value. For the range of Al volume fraction considered in this study, the Al species is the limiting factor determining the extent of heating, due to the Al fraction being under its balanced stoichiometric level. The average temperature within the microstructure also tends to a steady-state value, as the overall heating due to electrical and chemical dissipations is finite. To extrapolate and estimate this average steady-state temperature ($T_{SS}$) over the long time duration which is not reached by the simulations, the data points obtained for the simulation window are fitted to the empirical equation

$$\hat{T}(t) = T_0 + (T_{SS} - T_0)\sqrt{1 - \exp(-t/t_{ref})}, \quad (16)$$

where $T_0$ and $t_{ref}$ are the initial temperature (e.g., 293 K) and the reference time (80 ns is used), respectively. The equation allows the steady-state temperature $T_{SS}$ (i.e., the limit of $\hat{T}$ as $t \to \infty$) to be estimated without the need to run the simulations for a prolonged

14 March 2024 04:23:33
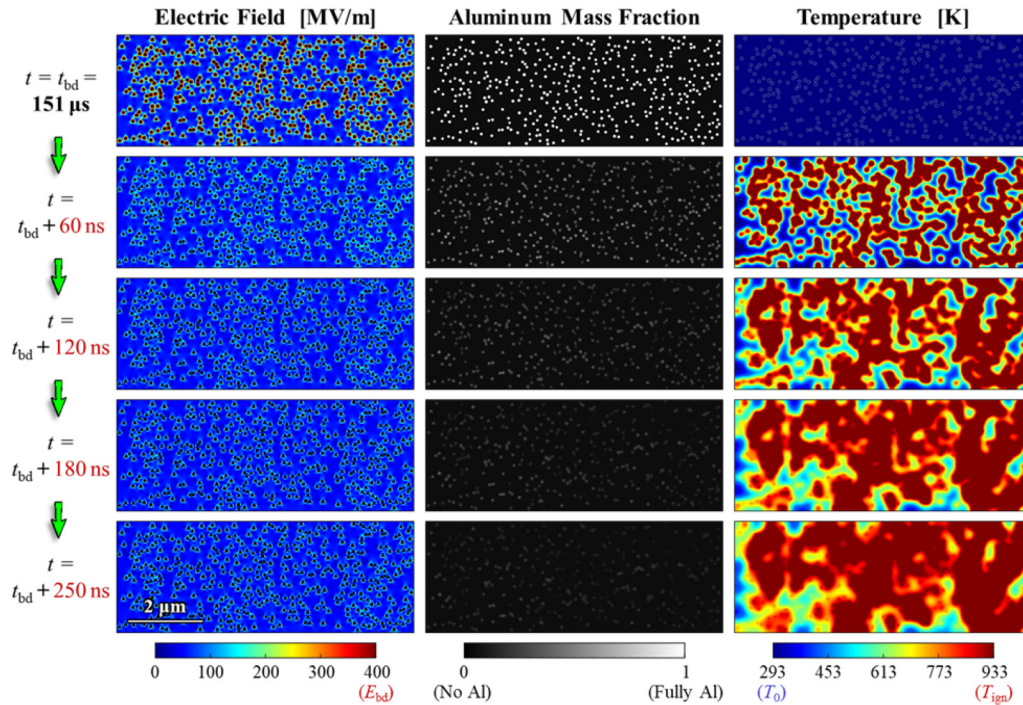
**FIG. 7.** Evolutions of *E*-field intensity (left), Al mass fraction (middle), and temperature (right) for the baseline microstructure subjected to $U_{in}$ = 1.16 GJ/m³ with breakdown initiation at $t_{bd}$ = 151 µs.

duration of time. In the analyses to follow, $T_{SS}$ is used as a measure to compare the response of different material and loading cases.

To assess the effects of transport and kinetic parameters on the reactive behavior, the average temperature in the baseline microstructure is analyzed in Fig. 10 through a parametric study. It is found that increasing the diffusion coefficient ($f$) yields higher temperatures. For example, under $U_{in}$ = 1.16 GJ/m³ with $t_{bd}$ = 151 µs, the average steady-state temperature ($T_{SS}$) increases from 932 to 947 K when the diffusion coefficients changes from 40% to 160% of the value referenced in Table II. Similarly, increasing the frequency factor ($A$) in the Arrhenius reaction rate also results in higher microstructural temperature, with $T_{SS}$ equal to 925 and 952 K for frequency factor values that are 40% and 160%, respectively, of the reference frequency factor ($A_{ref}$ = 7.524 × 10¹⁰ s⁻¹) under the same loading conditions.

The reason for the higher temperatures is due to the fact that transport and kinetic properties both play an important role in influencing the rate of chemical reaction (and hence, the heat dissipation). Specifically, faster diffusion or faster reaction kinetics leads to a higher extent of reaction. For instance, at the steady-state limit, the remaining Al fraction (as a percentage of its initial amount) in the baseline microstructure having a diffusion coefficient that is increased by 60% relative to $f_{ref}$ is only ~7%, while that having a diffusion coefficient that is decreased by 60% relative to $f_{ref}$ is ~25%. Similarly, the remaining Al fraction in the microstructure with a frequency factor 60% higher relative to $A_{ref}$ is only ~8%,

while that with a frequency factor 60% lower relative to $A_{ref}$ is ~15%. Such parametric studies offer insight into how the influence of individual material properties and uncertainties in their values may be analyzed explicitly.

## IV. QUANTIFICATION OF REACTIVITY

Consistent with the conventional definition employed by the scientific community, ignition is defined as the state at which the material can maintain a self-sustaining, exothermic chemical reaction. The critical condition necessary for ignition is satisfied when the rate of total heat generation (e.g., mechanical, electrical, chemical, and thermal) in the material is invariably greater than that of heat dissipation (e.g., thermal conduction). For P(VDF-TrFE)/nAl, DeLisio deduced from experiment[54,75] that this condition is practically met when the average temperature of the specimen is higher than its ignition temperature ($T_{ign}$ = 933 K). This temperature dependency is a consequence of the fact that the exothermic reaction is catalyzed by temperature increase in the material [see Eq. (8)]. The unstable, spiraling cycle of heat generated by chemistry eventually comes to a halt when one of the reactant species has been fully exhausted by the reaction.

Using this temperature-based criterion (i.e., $T_{SS} > T_{ign}$), the ignition time ($t_{ign}$, or the time it takes for reaction initiation after onset of loading) at a given load intensity ($U_{in}$) is analyzed and used as a relative means to compare the reactive response and
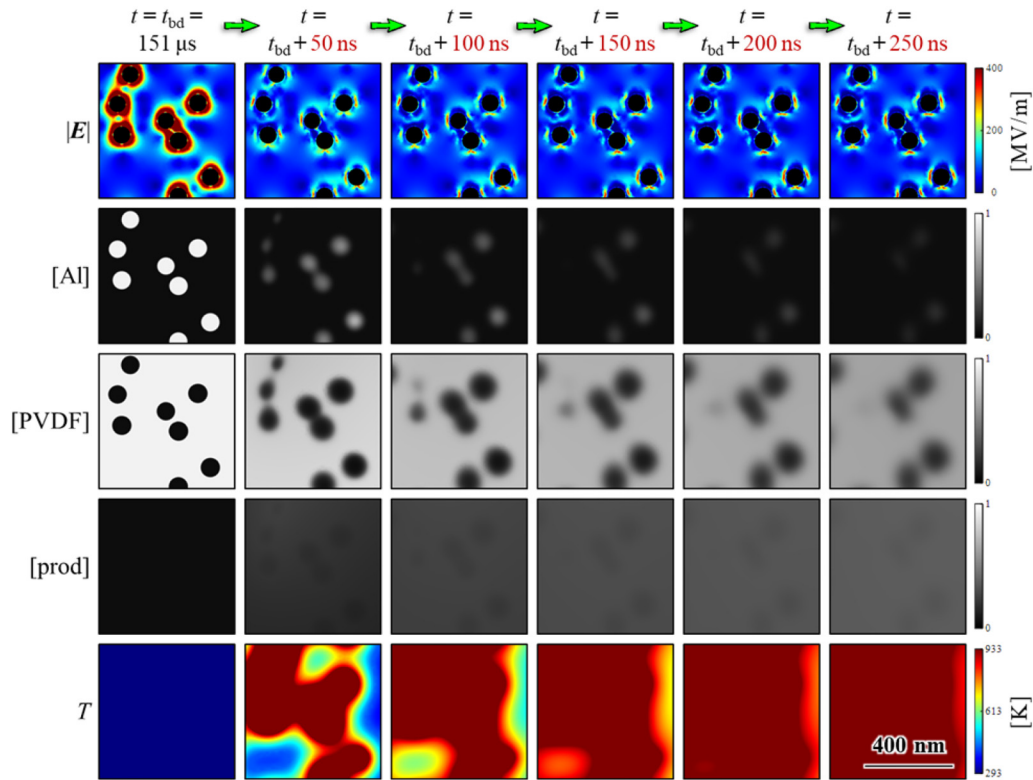
**FIG. 8.** Evolutions of E-field, chemical species, and temperature (inset view of the Al particles shown) throughout dielectric breakdown and exothermic reaction. The microstructure and loading conditions are same as those described in Fig. 7.
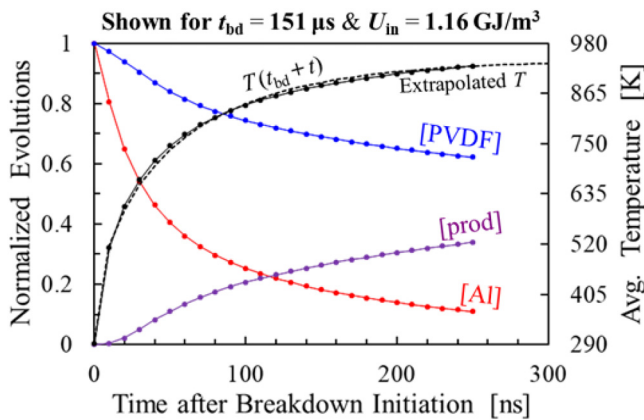
**FIG. 9.** Time histories of the average Al (red), PVDF (blue), product (purple) mass fractions, and temperature (black). Evolutions of the reactant species are normalized by their respective initial concentrations. The microstructure is the baseline microstructure, and the loading conditions are same as in Fig. 7.

sensitivity to ignition for different materials.[76–78] Here, $t_{ign}$ is defined as the time it takes for the average temperature to reach $T_{ign}$. As illustrated in Fig. 11, $t_{ign}$ for the microstructure set in Fig. 3 with $D_{A1} = 80$ nm, $\theta_{A1} = 9\%$, and no voids (this configuration is referred to as the *baseline* microstructure) ranges between 145.9 and 155.5 µs under $U_{in} = 1.16$ GJ/m³, due to microstructure heterogeneity fluctuations. The post-ignition behavior (e.g., deflagration) of the specimen, which typically involves much higher temperatures (close to the adiabatic flame temperature of ~1500 K[61]) is not modeled, as the focus is on predicting the conditions required for the initiation of self-sustaining reaction and the time different materials take to that state.

In Fig. 12, the time to reaction initiation (or ignition time, $t_{ign}$) is plotted for different load intensities ($U_{in}$) for the baseline configuration described above. As the $U_{in}$ is increased, $t_{ign}$ decreases. Obviously, the critical temperature ($T_{ign}$) required for the initiation of self-sustained exothermic reaction is attained more rapidly under a higher load intensity. A comparison between the experimental results and the simulation results confirms that $t_{ign}$ is generally in good agreement in terms of the overall magnitude and
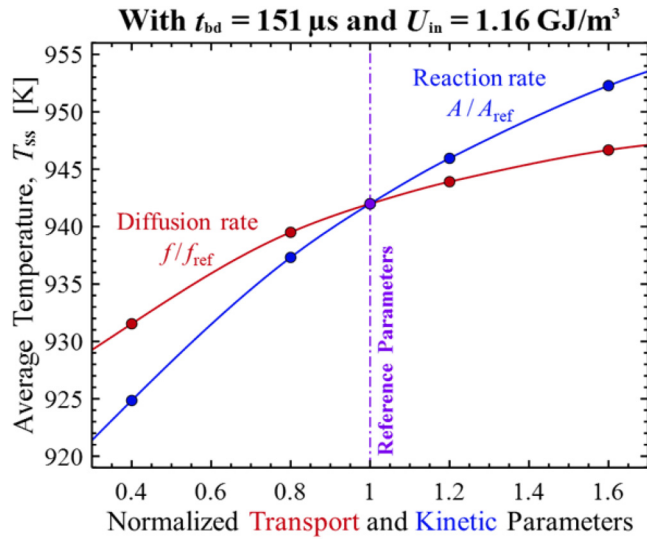
**FIG. 10.** Average temperature in the baseline microstructure ($U_{in}$ = 1.16 GJ/m$^3$, $t_{bd}$ = 151 μs) at different levels of diffusion coefficient (red) and frequency factor (blue). The parameters are normalized by their reference values (transport parameters listed in Table II).

trends. Both the calculated and experimentally measured trend can be well described by a phenomenological equation of the form

$$t_{ign} = (\alpha + \beta U_{in})^{-0.5}, \tag{17}$$
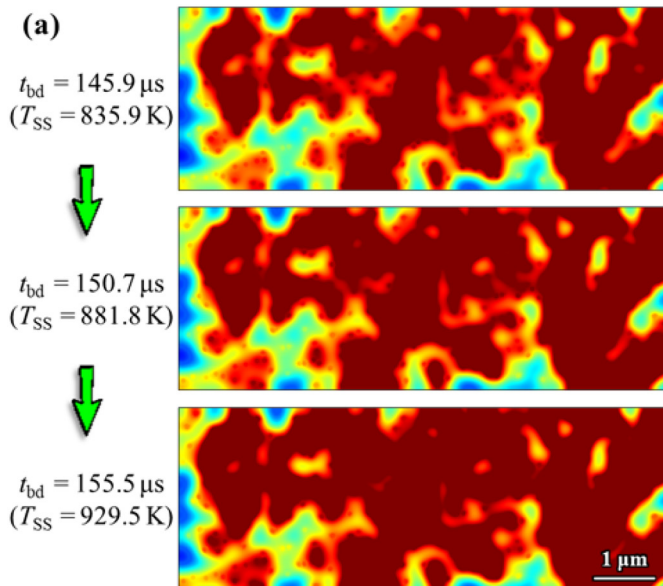
where $\alpha$ and $\beta$ are fitting coefficients. The ignition threshold ($U_{cr}$), or the minimum load intensity required for the initiation of self-sustaining, exothermic chemical reaction, can be also calculated by taking the limit of $t_{ign} \to \infty$, leading to $U_{cr} = -\alpha/\beta$. For instance, the ignition threshold of the baseline microstructure set is $U_{cr}$ = 0.61 GJ/m$^3$. This threshold is a material attribute and will be used in the analyses to come to compare the behaviors of different material cases later in this paper. Recognizing that the critical electrostatic energy density (at the onset of breakdown initiation) required for ignition is ~0.002 GJ/m$^3$ for the baseline microstructure (compared to $U_{cr}$ = 0.61 GJ/m$^3$), this implies that only a small fraction (~0.3%) of the input energy ($U_{in}$) is converted into heat generation via resistive heating. The vast remainder of the critical energy required for ignition is initially stored in the Al particles and is gradually dissipated into the material as chemical reaction progresses.

## A. Probabilistic analysis

It is useful to quantify the uncertainties in the reactivity of the HEMs, as random heterogeneity variations inherent in microstructures cause the material behavior to be stochastic. The dataset of the ignition times ($t_{ign}$) for each SEMSS over a range of load intensity is described using the Weibull distribution in Eq. (18) with parameters $w_1$ and $w_2$. The ignition probability ($P_{ign}$), or the likelihood of whether the critical condition for the initiation of self-sustaining, exothermic reaction is satisfied, is calculated as a function of time (since onset of loading) for each microstructural configuration and load intensity ($U_{in}$),

$$P_{ign}(t) = 1 - \exp[-(t/w_1)^{w_2}]. \tag{18}$$
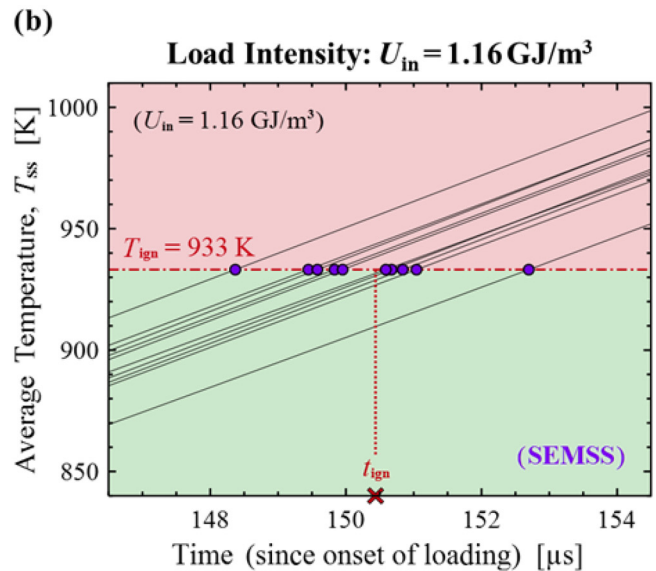


**FIG. 11.** (a) Temperature evolution for the baseline microstructure and loading conditions discussed in Fig. 7; (b) time history of the average $T_{SS}$ for the multiple random microstructure samples in the SEMSS for statistical analysis.
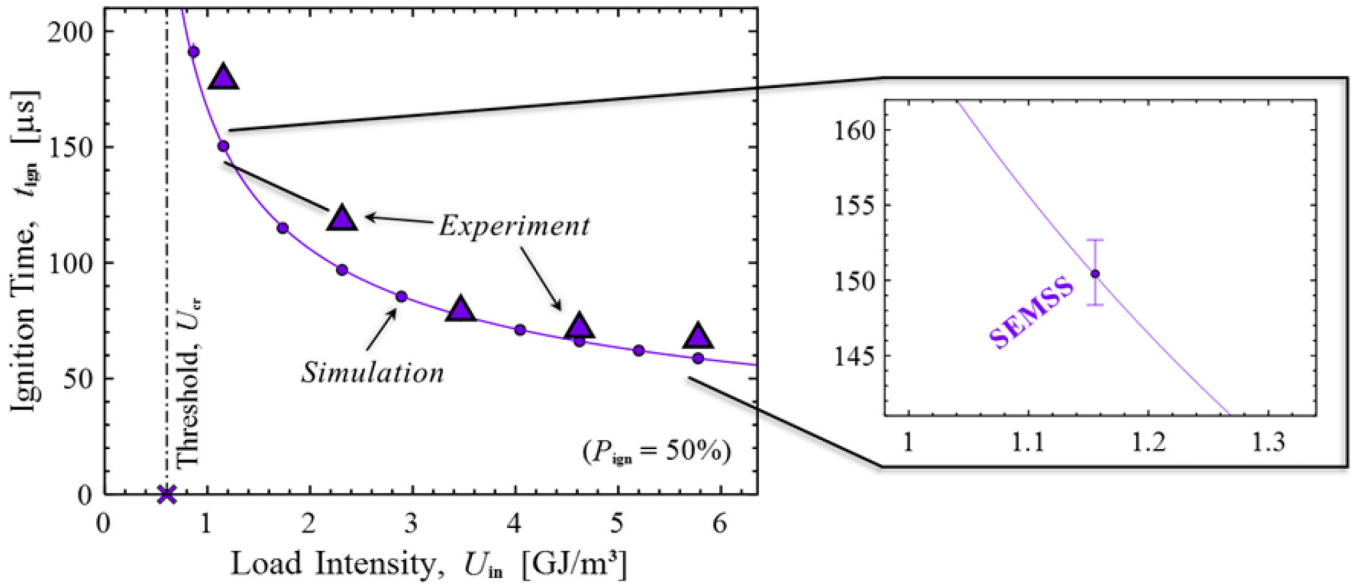
**FIG. 12.** Time to reaction initiation ($t_{ign}$) as a function of load intensity ($U_{in}$) obtained from simulations (circles) and measured in experiments (triangles). The results are for the baseline microstructure set shown in Fig. 3. The limit of $t_{ign}$ approaching infinity allows $U_{cr}$ to be established.

The effect of $U_{in}$ on $t_{ign}$ is shown in Fig. 13 for the baseline microstructure set. As $U_{in}$ is increased from 0.87 to 1.73 GJ/m$^3$, $t_{ign}$ (with $P_{ign} = 50\%$) decreases from 194.6 to 116.4 µs. $P_{ign}$ is calculated and shown in Fig. 14 for the baseline microstructure set. Here, the lower-left region below the curve (shaded in blue) represents the range of scenarios under which $P_{ign} < 50\%$. In contrast, the upper-right region (shaded in red) represents the case under which $P_{ign} > 50\%$. It can be seen that the resulting variation in the ignition probability is small, as the coefficient of variation (i.e.,

ratio of standard deviation to mean) of $t_{ign}$ is only ~2.4% for the baseline microstructure set.

## V. MICROSTRUCTURAL EFFECTS ON REACTIVITY

The mesoscale framework developed allows the reactive behavior of various microstructures to be analyzed systematically. As shown in Fig. 6, the microstructure attributes varied are particle size $D_{Al}$ (between 70 and 85 nm), particle volume fraction $\theta_{Al}$
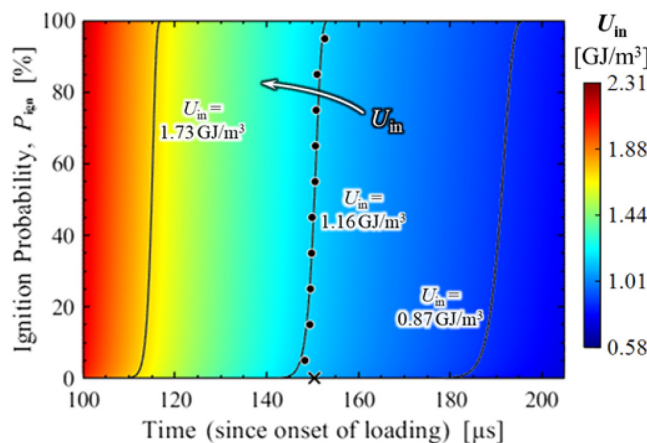


**FIG. 13.** Ignition probability in terms of time under different load intensities for the baseline microstructure set shown in Fig. 3.
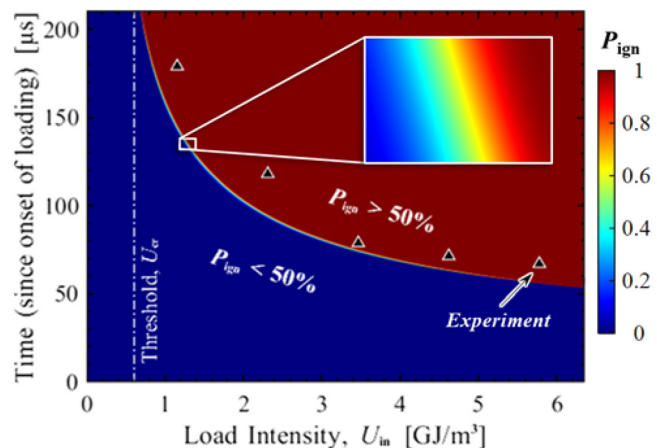


**FIG. 14.** Colormap showing $P_{ign}$ as a function of $U_{in}$ and time for the baseline microstructure set. The black triangles denote experimental measurements.[53]

(between 7% and 11%), void size $D_{vd}$ (between 100 and 200 nm), porosity $\theta_{vd}$ (between 0% and 10%), and particle dispersity $\xi_{Al}$ (between 0.65 and 1.49). Each microstructure setting involves ten random instantiations to allow statistical variations in behavior to be quantified.

First, the effect of particle size ($D_{Al}$) on the rate of hotspot formation, which is responsible for the initiation of exothermic reaction, is illustrated in Figs. 15 and 16. The two microstructure sets shown have a particle volume fraction of $\theta_{A1} = 9\%$ and are non-porous ($\theta_{vd} = 0\%$). Compared to $t_{ign} = 150.4\,\mu s$ for the baseline microstructure ($D_{Al} = 80$ nm), $t_{ign}$ for the smaller particle size case ($D_{A1} = 70$ nm) is $139.6\,\mu s$, representing an ~7% difference. The quicker reaction initiation observed in the smaller particle size case can be attributed to several effects,[79–81] including (i) stronger local fields near the particles which lead to higher hotspot temperatures upon breakdown [see Figs. 6(a) and 6(b)]; and more importantly, (ii) enhanced mixing of the reactant species through interdiffusion across the smaller particles. These factors facilitate a faster and more complete reaction. To put this in perspective, the ratio of Al species remaining in the microstructure at $t = 133\,\mu s$ to the initial Al mass fraction is 0.125 for the smaller particle case ($D_{A1} = 70$ nm), while that for the larger particle case ($D_{A1} = 80$ nm) is 0.217 under the same loading conditions.

Similarly, the effect of particle volume fraction ($\theta_{Al}$) is shown in Figs. 17 and 18. For both microstructure sets shown, the mean particle size is $D_{A1} = 80$ nm and there are no voids. The time to reaction initiation ($t_{ign}$) for $\theta_{A1} = 7\%$ case is $173.3\,\mu s$, while that for the baseline microstructure set ($\theta_{A1} = 9\%$) is $150.4\,\mu s$. The slower reaction initiation (by ~15%) in the lower $\theta_{Al}$ case[82] is primarily due to (i) the lower amount of energy available in the Al particles (by ~22%) and (ii) decreased reactant mixing due to longer mean interparticle distances.

The effect of porosity ($\theta_{vd}$), or void volume fraction, is analyzed in Figs. 19 and 20. Both cases have $D_{A1} = 80$ nm and $\theta_{A1} = 9\%$. Relative to that for the baseline case, the ignition time for the porous case (with $\theta_{vd} = 5\%$ and $D_{Vd} = 150$ nm) is $134.5\,\mu s$, representing a reaction initiation that is ~11% quicker. While voids themselves do not give rise to hotspots directly, voids can enhance the neighboring local fields,[83] which lead to more intense hotspots (see Fig. 19), and reduce the amount of material that need to be heated, thereby accelerating the overall heating of the microstructure and consequently, the onset of chemical reaction.

Lastly, the effect of particle dispersity ($\xi_{Al}$) on hotspot development is analyzed and shown in Figs. 21 and 22. In both cases, $D_{A1} = 80$ nm and $\theta_{A1} = 9\%$. For the case with well-dispersed Al particles ($\xi_{Al} = 1.49$), $t_{ign}$ is $145.1\,\mu s$, which is ~4% slower relative to
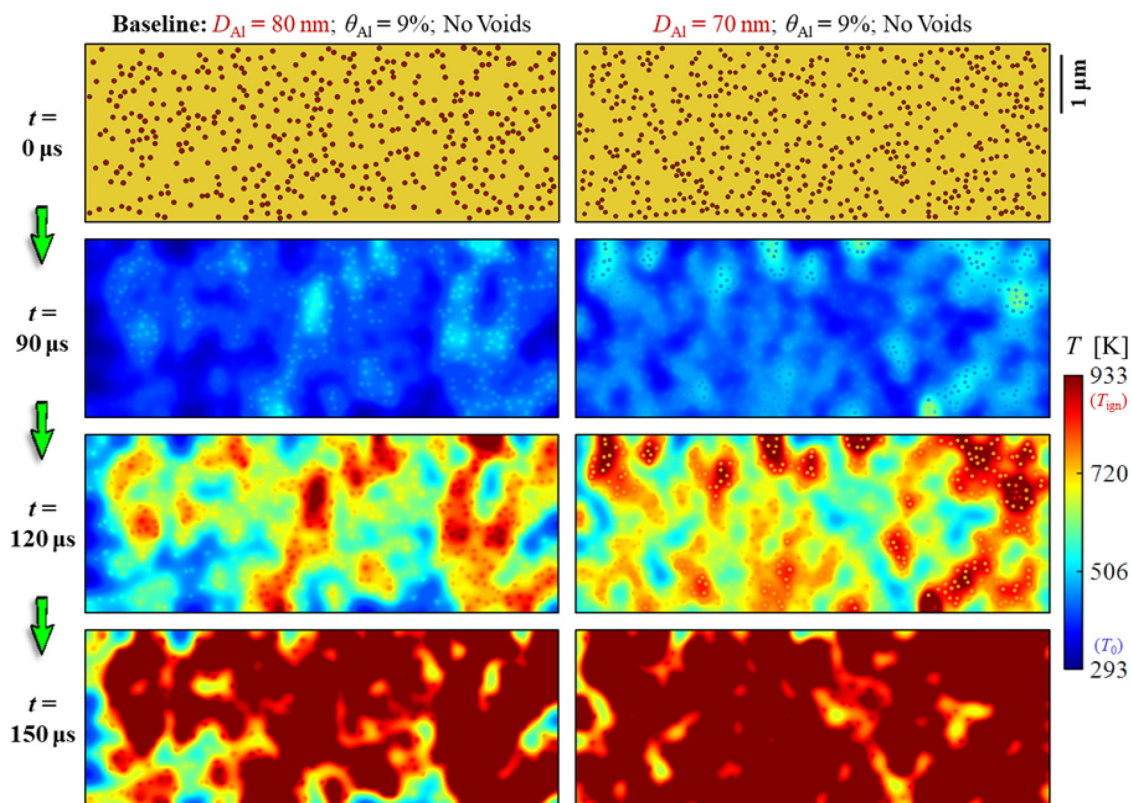


**FIG. 15.** Evolutions of temperature in microstructures with particle size $D_{Al} = 80$ nm (left) and 70 nm (right). Both are non-porous with $\theta_{Al} = 9\%$. The load intensity is $U_{in} = 1.16$ GJ/m³.
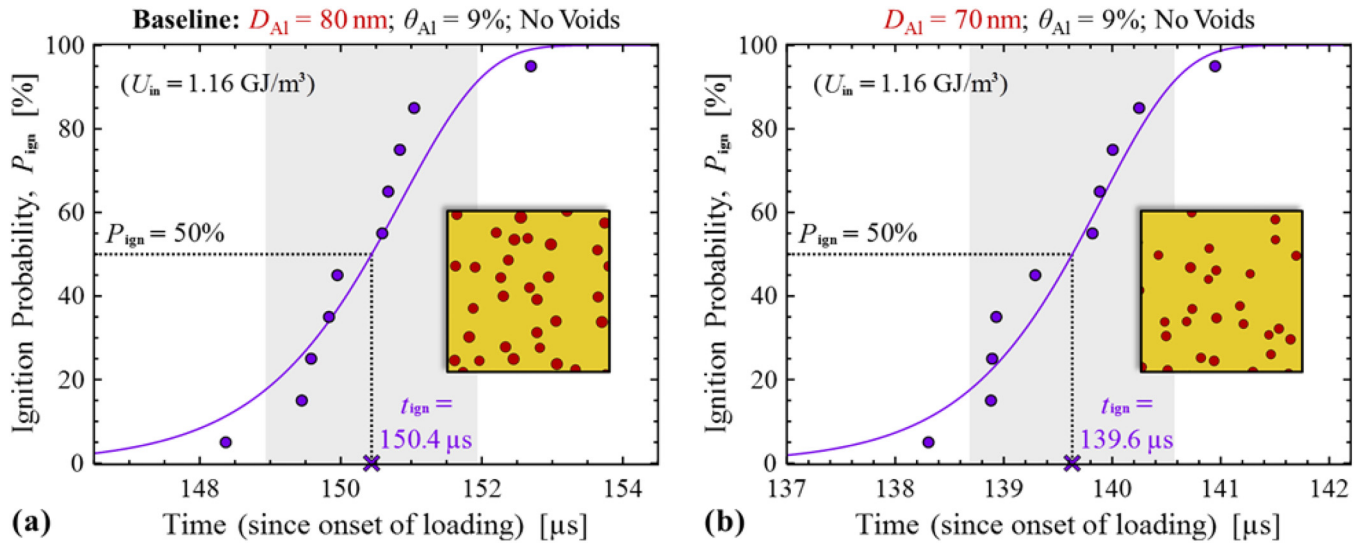
**FIG. 16.** $P_{ign}$ as a function of time for $D_{Al}$ = (a) 80 nm and (b) 70 nm with $\theta_{Al}$ = 9%, $\theta_{vd}$ = 0% (non-porous), $U_{in}$ = 1.16 GJ/m³. The shaded region (gray) indicates the standard deviation.



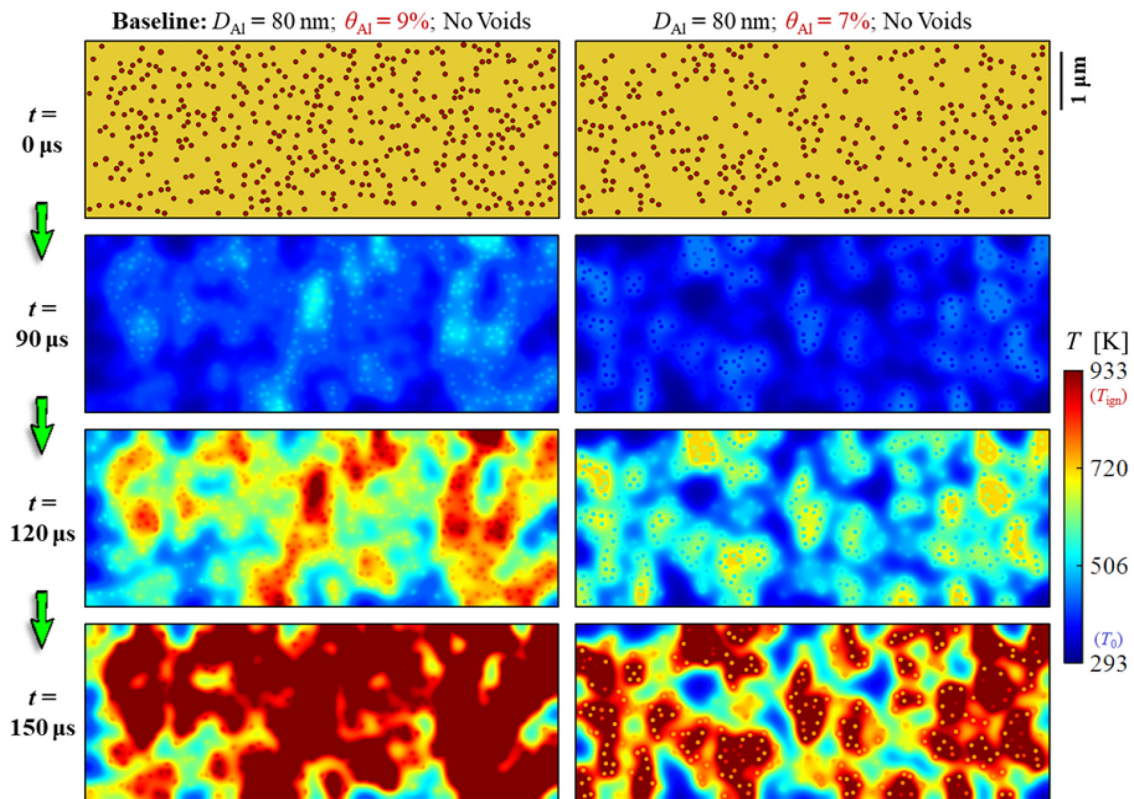**FIG. 17.** Evolutions of temperature in microstructures with particle volume fraction $\theta_{Al}$ = 9% (left) and 7% (right). Both are non-porous with $D_{Al}$ = 80 nm. The load intensity is $U_{in}$ = 1.16 GJ/m³.
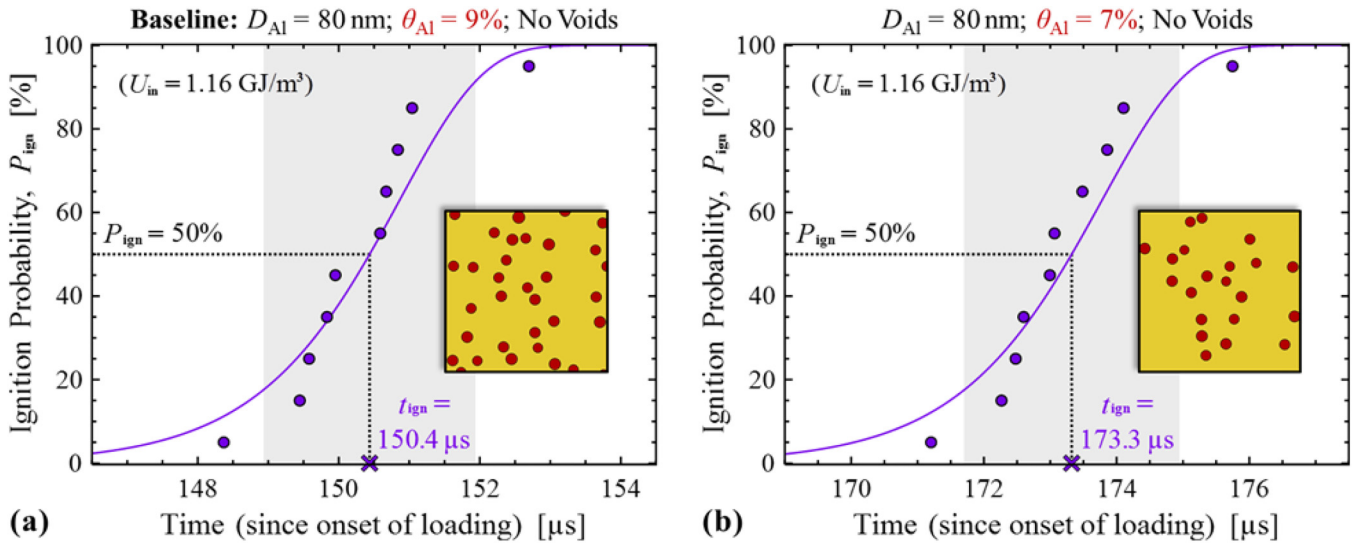
**FIG. 18.** $P_{ign}$ as a function of time for $\theta_{Al}$ of (a) 9% and (b) 7% with $D_{Al}$ = 80 nm, $\theta_{vd}$ = 0% (non-porous), $U_{in}$ = 1.16 GJ/m³. The shaded region (gray) indicates the standard deviation.



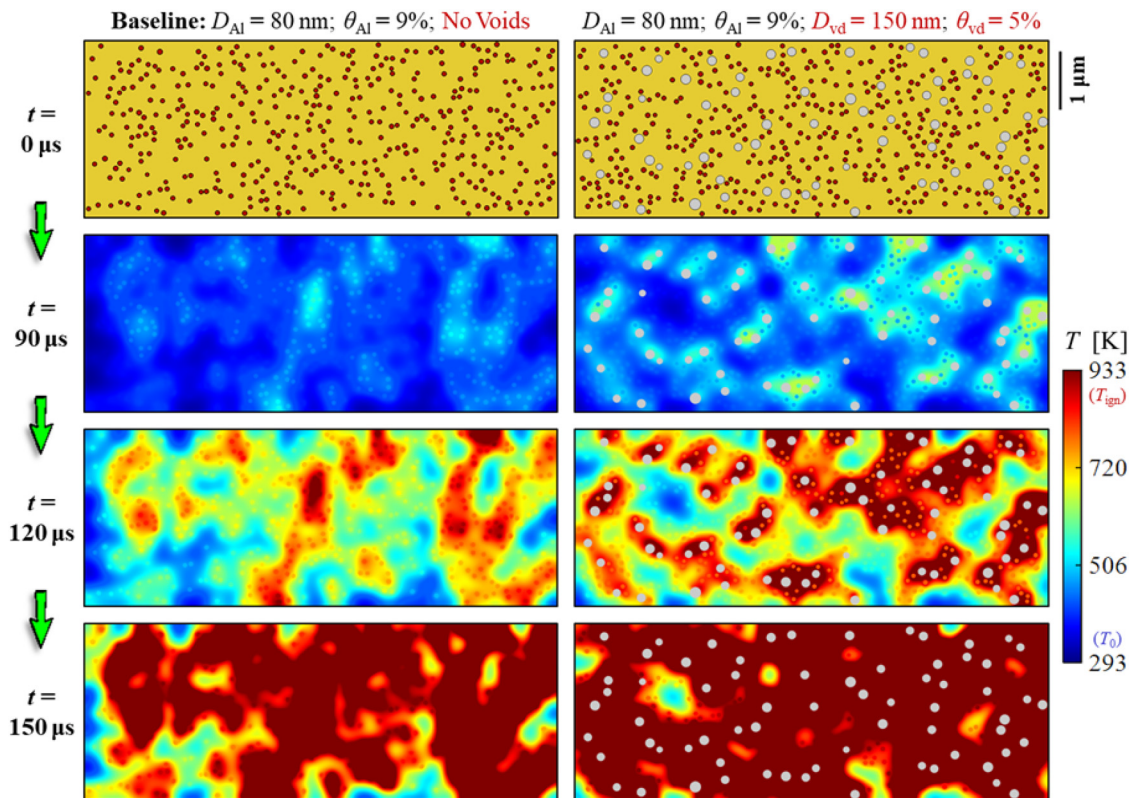**FIG. 19.** Evolutions of temperature in microstructures with porosity $\theta_{vd}$ = 0% (left) and 5% (right). Both have $D_{Al}$ = 80 nm and $\theta_{Al}$ = 9%. The porous case has void size $D_{vd}$ = 150 nm. The load intensity is $U_{in}$ = 1.16 GJ/m³.
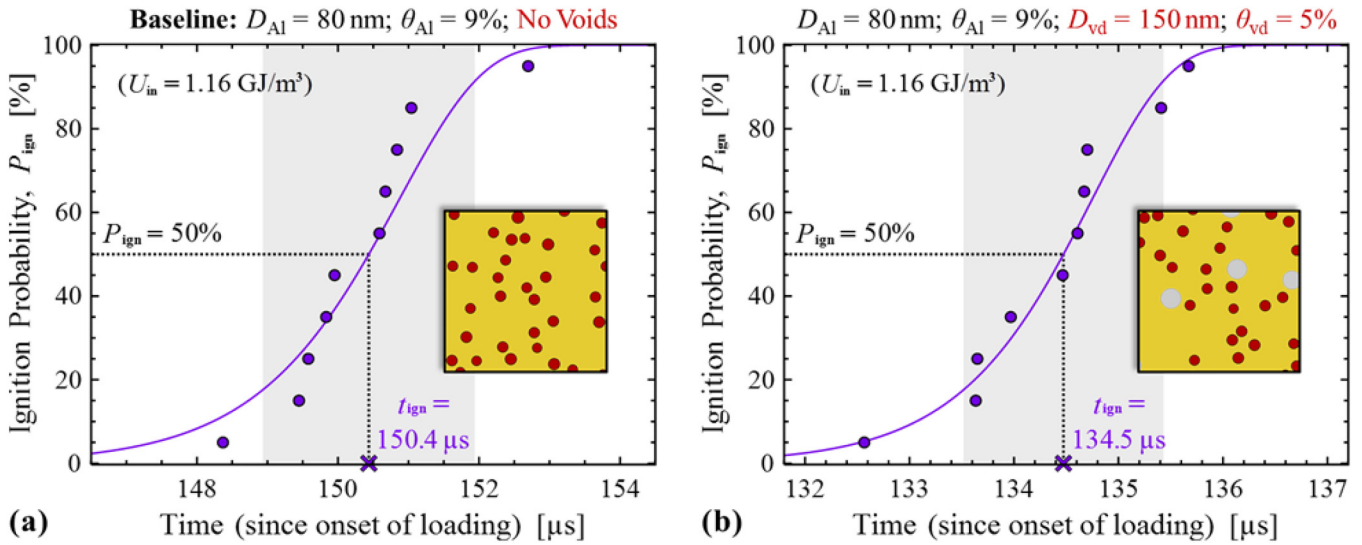
**FIG. 20.** $P_{ign}$ as a function of time for $\theta_{vd}$ = (a) 0% and (b) 5% with $D_{Al}$ = 80 nm, $\theta_{Al}$ = 9%, and $D_{vd}$ = 150 nm, $U_{in}$ = 1.16 GJ/m³. The shaded region (gray) indicates the standard deviation.
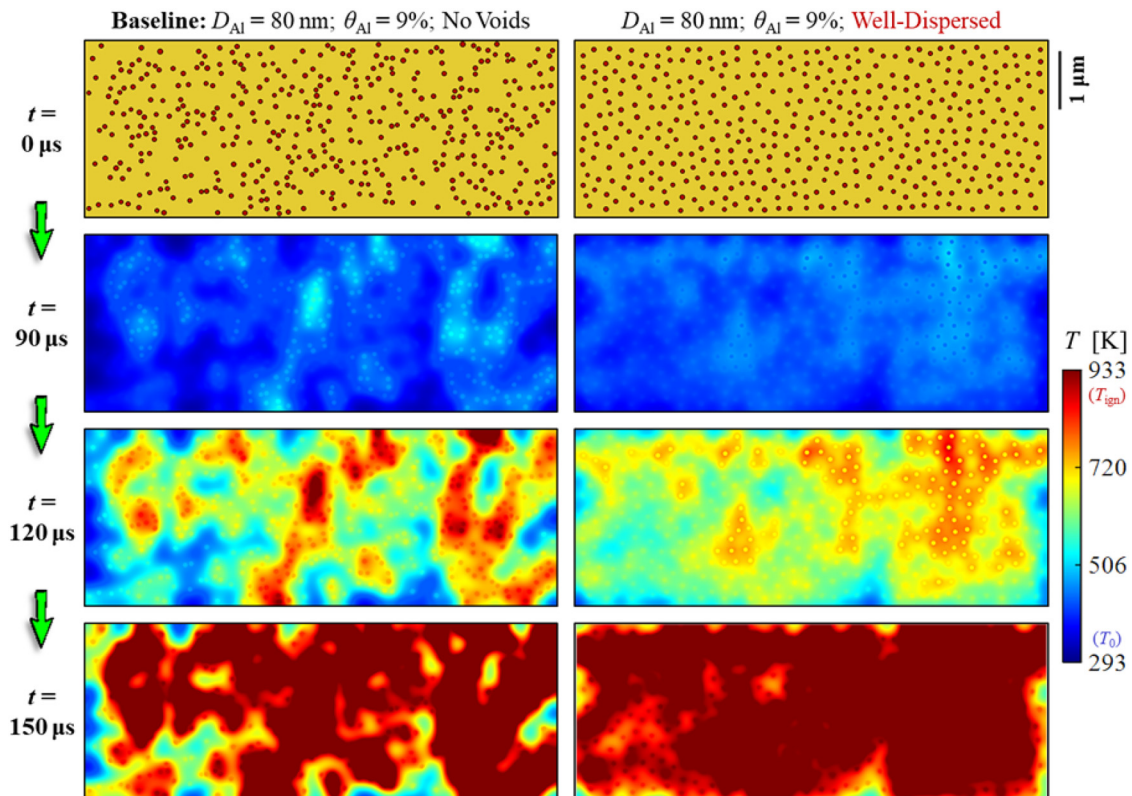


**FIG. 21.** Evolutions of temperature in microstructures with particle dispersity $\xi_{Al}$ = 0.65 (left) and $\xi_{Al}$ = 1.49 (right). Both are non-porous with $D_{Al}$ = 80 nm and $\theta_{Al}$ = 9%. The load intensity is $U_{in}$ = 1.16 GJ/m³.

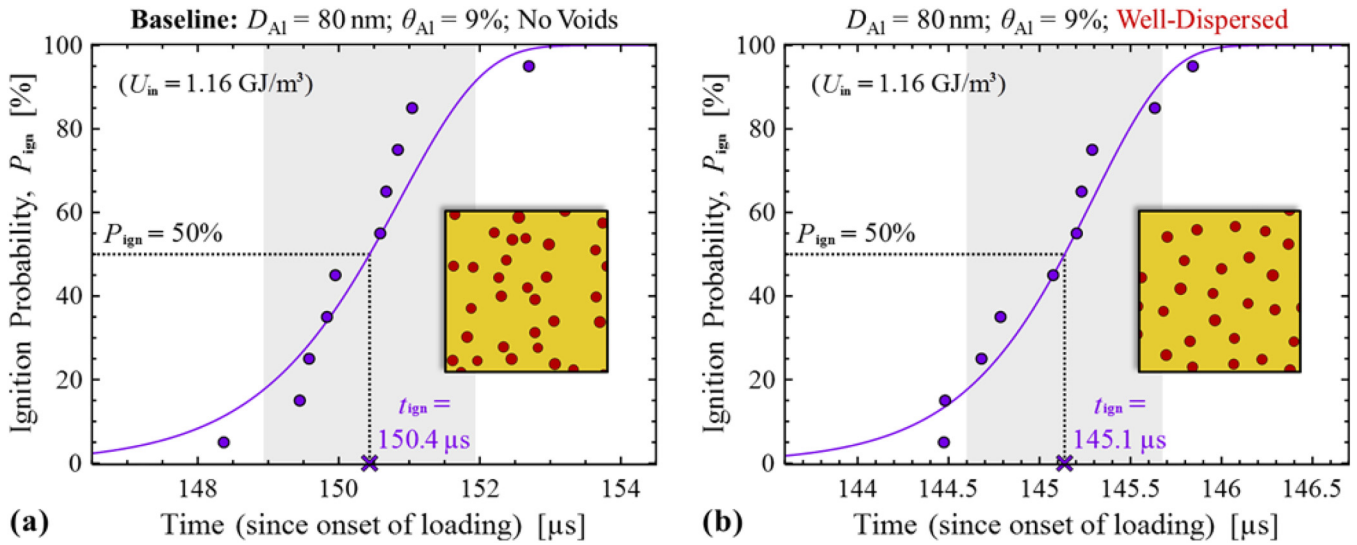**FIG. 22.** $P_{ign}$ as a function of time for $\xi_{Al}$ (a) 0.65 and (b) 1.49 with $D_{Al}$ = 80 nm, $\theta_{Al}$ = 9%, $\theta_{vd}$ = 0%, $U_{in}$ = 1.16 GJ/m$^3$. The shaded region (gray) indicates the standard deviation.
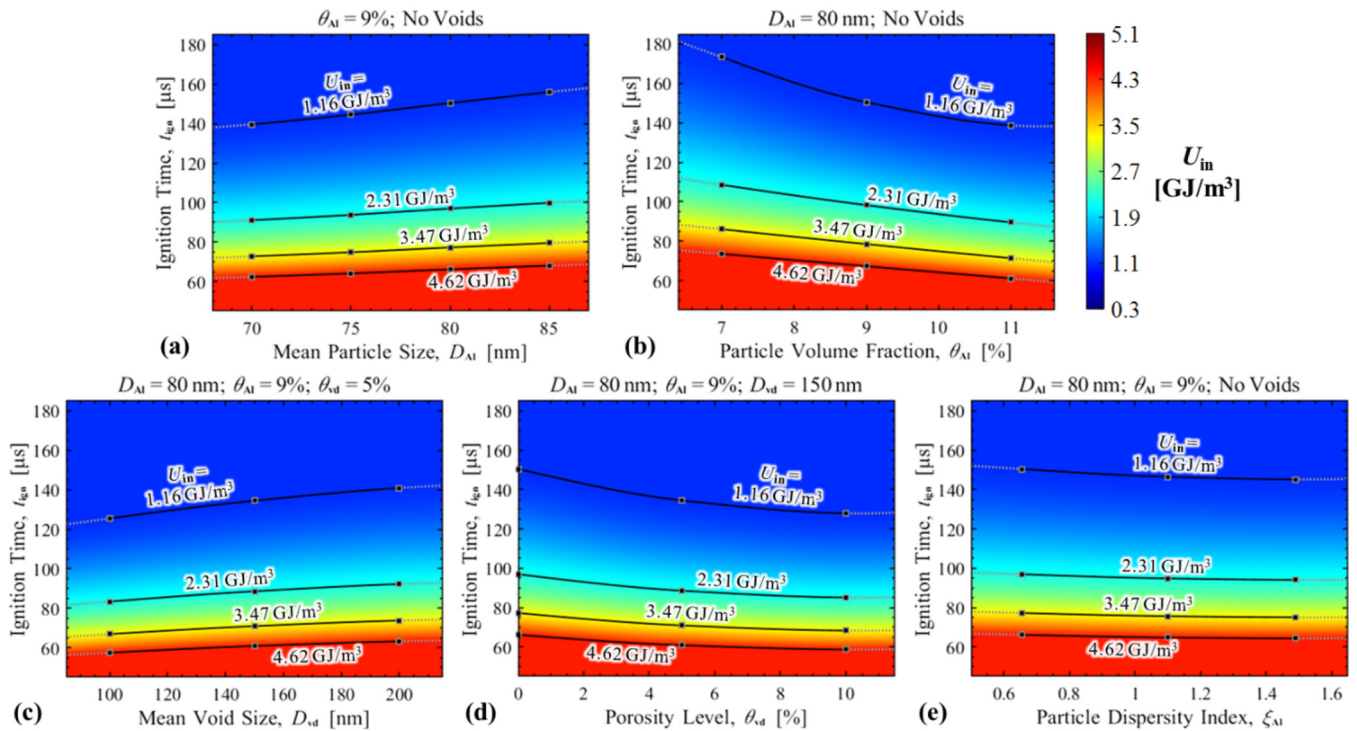


**FIG. 23.** Ignition time as a function of $U_{in}$ and different levels of (a) $D_{Al}$, (b) $\theta_{Al}$, (c) $D_{vd}$, (d) $\theta_{vd}$, and (e) $\xi_{Al}$.
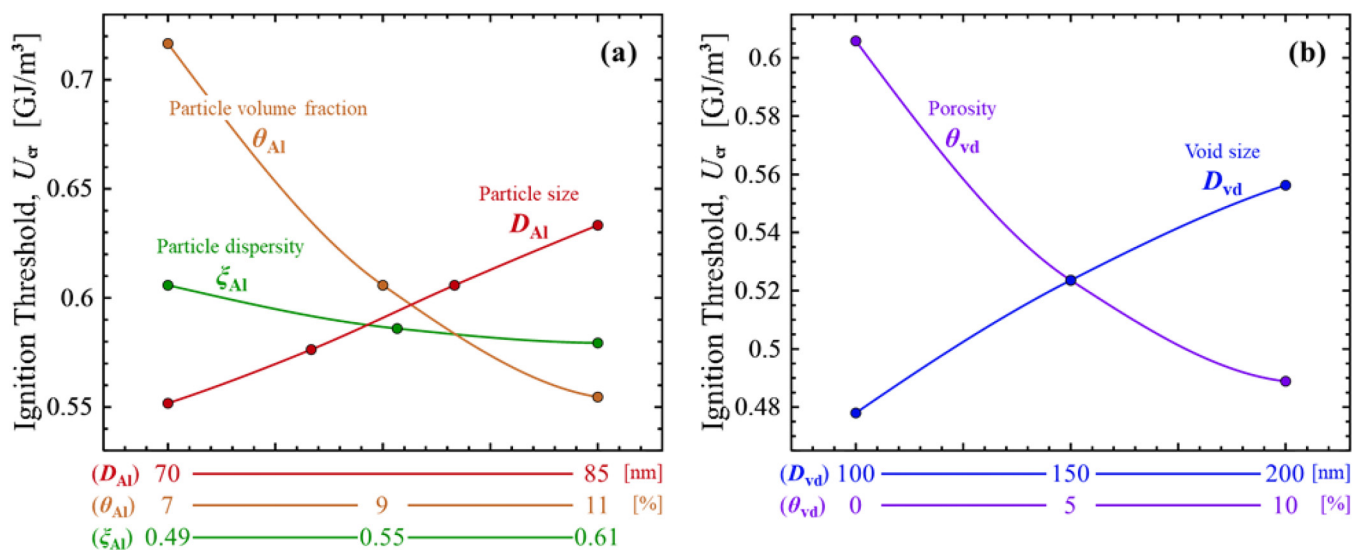
**FIG. 24.** Summary of ignition thresholds for the different microstructure sets analyzed with varying levels of (a) particle size, particle volume fraction, and particle dispersity; (b) void size and porosity.

the baseline case shown in Fig. 3 ($\xi_{Al} = 0.65$). This increased reaction rate caused by particle dispersity is due to the smaller interparticle distances which facilitate reactant mixing and thermal transport.

The influences of the above factors on the times to reaction initiation ($t_{ign}$) are summarized in Fig. 23 for a range of load intensities ($U_{in}$). Clearly, larger particle and void sizes lead to slower reaction development. In contrast, higher volume fractions of Al particles and voids result in faster reaction initiation. Particle dispersity can also influence the reaction process as shown.

The ignition threshold ($U_{cr}$), or the critical load intensity required for self-sustaining, exothermic chemical reaction, is taken as a measure of reaction sensitivity and analyzed in Fig. 24. Large

particle and void sizes lead to higher ignition thresholds or lower sensitivity (e.g., $U_{cr} = 0.63$ and $0.55\,GJ/m^3$ for $D_{A1} = 85$ and 70 nm, respectively) for reasons already stated. On the other hand, microstructures with higher volume fractions of particles or voids have lower ignition thresholds and higher sensitivity (e.g., $U_{cr} = 0.55$ and $0.72\,GJ/m^3$ for $\theta_{A1} = 11\%$ and 7%, respectively). The Weibull parameters and the ignition threshold for each of the twelve microstructure sets are summarized in Table III. While ignition threshold is a useful measure of reaction sensitivity in general, the time to reaction initiation ($t_{ign}$) is useful when comparing the macroscopic reactivity of materials with different microstructures under the same loading conditions.

## VI. CONCLUSIONS

A mesoscale framework for simulating the initiation and development of reaction in heterogeneous energetic materials is developed. As illustrated in Figs. 1 and 2, this framework explicitly captures the microstructure, interdiffusion between the reactants, advection of the species mixture, and chemical kinetics of the reaction used to predict the reactive behavior of materials at the macroscale. An Arrhenius relation is used to capture the rate of reactive heat release. The quantification of uncertainties in predicted material behavior due to stochastic fluctuations in microstructural heterogeneities is an intrinsic part of the framework, because multiple statistically equivalent microstructure instantiations are considered in a manner similar to the use of multiple samples in experiments. In the calculations carried out, the focus has been on the evolution process of reaction in a composite of poly(vinylidene fluoride-co-trifluoroethylene) and nanoaluminum [or P(VDF-TrFE)/nAl]. Microstructural effects including particle size, void size, particle volume fraction, porosity, and particle dispersity are analyzed

**TABLE III.** Summary of Weibull parameters and ignition thresholds.

| $D_{Al}$ (nm) | $\theta_{Al}$ (%) | $\xi_{Al}$ | $D_{vd}$ (nm) | $\theta_{vd}$ (%) | $w_1$ (μs) | $w_2$ (μs) | $U_{cr}$ (GJ/m³) |
|---|---|---|---|---|---|---|---|
| 80 | 9 | 0.65 | … | 0 | 150.9 | 127.1 | 0.61 |
| 70 | 9 | … | … | 0 | 139.9 | 188.4 | 0.55 |
| 75 | 9 | … | … | 0 | 144.9 | 13.8 | 0.58 |
| 85 | 9 | … | … | 0 | 156.3 | 178.8 | 0.63 |
| 80 | 7 | … | … | 0 | 173.8 | 136.3 | 0.72 |
| 80 | 11 | … | … | 0 | 139.0 | 153.2 | 0.55 |
| 80 | 9 | … | 100 | 5 | 125.7 | 259.0 | 0.48 |
| 80 | 9 | … | 150 | 5 | 134.7 | 178.8 | 0.52 |
| 80 | 9 | … | 200 | 5 | 141.2 | 168.9 | 0.56 |
| 80 | 9 | … | 150 | 10 | 128.0 | 337.4 | 0.49 |
| 80 | 9 | 1.10 | … | 0 | 146.6 | 397.6 | 0.59 |
| 80 | 9 | 1.49 | … | 0 | 145.3 | 344.1 | 0.58 |

systematically. The mesoscale simulations allowed the macroscopic ignition responses of the materials to be predicted as a function of microstructural attributes. In particular, the ignition threshold (i.e., minimum load intensity required to cause ignition) and the time to ignition under a given load intensity are quantified. It is found that microstructural variations can be used to alter the reactive responses of the material system. The trends obtained from the computational analyses are in qualitative agreement with reported trends in the literature. Calculations are also carried out to explore the effects of physical parameters at the mesoscale. Specifically, it is found that interdiffusion and the chemical kinetics play important roles in the reaction rate.

For the particular material system analyzed, the mechanism responsible for the initial microstructural heating and subsequently the onset of exothermic reactive processes is the dielectric breakdown initiated by the development of electric field via piezoelectricity and flexoelectricity. As such, the model resolves the breakdown process as well as the diffusion, advection, and exothermic reaction processes simultaneously. Although the particular hotspot-inducing mechanism considered is dielectric breakdown here, the framework is applicable for analyzing the reaction initiation and propagation and to establish microstructure-–reaction relations under different types of stimuli, such as thermomechanical inelastic dissipation, frictional heating, and laser or microwave heating.

## ACKNOWLEDGMENTS

## AUTHOR DECLARATIONS

### Conflict of Interest

The authors have no conflicts to disclose.

### Author Contributions

**Ju Hwan (Jay) Shin:** Conceptualization (equal); Data curation (lead); Formal analysis (lead); Investigation (lead); Methodology (lead); Validation (equal); Writing – original draft (lead); Writing – review & editing (lead). **Min Zhou:** Conceptualization (equal); Funding acquisition (equal); Investigation (equal); Methodology (equal); Resources (equal); Software (equal); Supervision (equal); Validation (equal); Writing – original draft (equal); Writing – review & editing (equal).

## DATA AVAILABILITY

The data that support the findings of this study are available from the corresponding author upon reasonable request.

## REFERENCES

[1]D. H. Liebenberg, R. W. Armstrong, and J. J. Gilman, *Structure and Properties of Energetic Materials* (Materials Research Society, Pittsburgh, PA, 1993).

[2]G. A. Olah and D. R. Squire, *Chemistry of Energetic Materials* (Academic Press, 2012).

[3]P. F. Pagoria, G. S. Lee, A. R. Mitchell, and R. D. Schmidt, "A review of energetic materials synthesis," Thermochim. Acta **384**, 187 (2002).

[4]B. F. Henson, B. W. Asay, L. B. Smilowitz, and P. M. Dickson, "Ignition chemistry in HMX from thermal explosion to detonation," AIP Conf. Proc. **620**, 1069 (2002).

[5]S. H. Fischer and M. C. Grubelich, *Theoretical Energy Release of Thermites, Intermetallics, and Combustible Metals* (Sandia National Lab, Albuquerque, NM, 1998).

[6]C. Milanese, F. Maglia, A. Tacca, U. Anselmi-Tamburini, C. Zanotti, and P. Giuliani, "Ignition and reaction mechanism of Co–Al and Nb–Al intermetallic compounds prepared by combustion synthesis," J. Alloys Compd. **421**, 156 (2006).

[7]M. T. Beason, I. E. Gunduz, and S. F. Son, "The role of fracture in the impact initiation of Ni-Al intermetallic composite reactives during dynamic loading," Acta Mater. **133**, 247 (2017).

[8]D. Reese, L. J. Groven, S. F. Son, and A. Mukasyan, "Intermetallic compounds as fuels for composite rocket propellants," in *47th AIAA/ASME/SAE/ASEE Joint Propulsion Conference & Exhibit* (AIAA, 2011), p. 5865.

[9]G. Lu, P. Li, Z. Liu, J. Xie, C. Ge, and H. Wang, "Theoretical model for the impact-initiated chemical reaction of Al/PTFE reactive material," Materials **15**, 5356 (2022).

[10]S. K. Valluri, M. Schoenitz, and E. L. Dreizin, "Ignition mechanisms of reactive nanocomposite powders combining Al, B, and Si as fuels with metal fluorides as oxidizers," Combust. Sci. Technol. **195**, 597 (2023).

[11]C. Dhandapani, G. Blanquart, A. C. Karp, E. T. Jens, and J. Rabinovitch, "Combustion studies of MMA/GOx for a hybrid rocket motor," Combust. Flame **256**, 112994 (2023).

[12]D. I. Pineda, L. Paxton, N. Perakis, C. Wei, S. Luna, H. Kahouli, M. Ihme, F. N. Egolfopoulos, and R. M. Spearrin, "Carbon oxidation in turbulent premixed jet flames: A comparative experimental and numerical study of ethylene, n-heptane, and toluene," Combust. Flame **221**, 371 (2020).

[13]E. F. Gittings, "Initiation of a solid explosive by a short-duration shock," in *Fourth Symposium (International) on Detonation* (Office of Naval Research-Department of the Navy, Washington, DC, 1965), Vol. 126, p. 373.

[14]B. D. Trott and R. G. Jung, "Effect of pulse duration on the impact sensitivity of solid explosives," in *Fifth Symposium on Detonation* (Office of Naval Research, Arlington, VA, 1970), Vol. 184, p. 191.

[15]R. C. Weingart, R. K. Jackson, C. A. Honodel, and R. S. Lee, "Shock initiation of PBX-9404 by electrically driven flyer plates, propellants, explosives," Pyrotechnics **5**, 158 (1980).

[16]M. R. Baer, "Mesoscale modeling of shocks in heterogeneous reactive materials," in *Shockwave Science and Technology Reference Library*, edited by Y. Horie (Springer, 2007), pp. 321–356.

[17]Y. Wei, C. Miller, D. Olsen, and M. Zhou, "Prediction of probabilistic shock initiation thresholds of energetic materials through evolution of thermal-mechanical dissipation and reactive heating," J. Appl. Mech. **88**, 091005 (2021).

[18]D. E. Kittell, C. D. Yarrington, J. B. Lechman, D. L. Damm, and M. R. Baer, "'Modelling the fluctuations of reactive shock waves in heterogeneous solid explosives as stochastic processes,' propellants, explosives," Pyrotechnics **45**, 295 (2020).

[19]Y. Wei, R. Ranjan, U. Roy, J. H. Shin, S. Menon, and M. Zhou, "Integrated Lagrangian and Eulerian 3D microstructure-explicit simulations for predicting macroscopic probabilistic SDT thresholds of energetic materials," Comput. Mech. **64**, 547 (2019).

[20]N. K. Rai, S. P. Koundinyan, O. Sen, I. V. Schweigert, B. F. Henson, and H. S. Udaykumar, "Evaluation of reaction kinetics models for meso-scale simulations of hotspot initiation and growth in HMX," Combust. Flame **219**, 225 (2020).

[21]M. W. Beckstead, Y. Liang, and K. V. Pudduppakkam, "Numerical simulation of single aluminum particle combustion," Combust., Explos. Shock Waves **41**, 622 (2005).

[22]Y. Gao, W. Zhu, T. Wang, D. E. Yilmaz, and A. C. T. Van Duin, "C/H/O/F/Al ReaxFF force field development and application to study the condensed-phase

poly(vinylidene fluoride) and reaction mechanisms with aluminum," J. Phys. Chem. C **126**, 11058 (2022).

[23] D. Q. Zhang, D. W. Wang, J. Yuan, Q. L. Zhao, Z. Y. Wang, and M. S. Cao, "Structural and electrical properties of PZT/PVDF piezoelectric nanocomposites prepared by cold-press and hot-press routes," Chin. Phys. Lett. **25**, 4410 (2008).

[24] T. Yamada, T. Ueda, and T. Kitayama, "Piezoelectricity of a high-content lead zirconate titanate/polymer composite," J. Appl. Phys. **53**, 4328 (1982).

[25] D. Chen, T. Sharma, and J. X. J. Zhang, "Mesoporous surface control of PVDF thin films for enhanced piezoelectric energy generation," Sens. Actuators, A **216**, 196 (2014).

[26] M. Zhang, D. Yan, J. Wang, and L. H. Shao, "Ultrahigh flexoelectric effect of 3D interconnected porous polymers: Modelling and verification," J. Mech. Phys. Solids **151**, 104396 (2021).

[27] X. Zhao, S. Zheng, and Z. Li, "Effects of porosity and flexoelectricity on static bending and free vibration of AFG piezoelectric nanobeams," Thin-Walled Struct. **151**, 106754 (2020).

[28] S. Chen, D. Y. Tang, X. X. Zhang, J. Y. Lyu, W. He, P. Liu, and Q. L. Yan, "Enhancing the combustion performance of metastable Al/AP/PVDF nanocomposites by doping with graphene oxide," Engineering **6**, 1019 (2020).

[29] C. Wang, M. Qin, Z. Yi, H. Deng, J. Wang, Y. Sun, G. Luo, and Q. Shen, "Oxidation mechanism of core-shell structured Al@PVDF powders synthesized by solvent/non-solvent method," Materials **15**, 3036 (2022).

[30] D. W. Kim, K. T. Kim, D. U. Lee, S. H. Jung, D. Y. Yang, and J. Yu, "Influence of poly(vinylidene fluoride) coating layer on exothermic reactivity and stability of fine aluminum particles," Appl. Surf. Sci. **551**, 149431 (2021).

[31] S. Appalakondaiah, G. Vaitheeswaran, and S. Lebègue, "A DFT study on structural, vibrational properties, and quasiparticle band structure of solid nitromethane," J. Chem. Phys. **138**, 184705 (2013).

[32] S. Appalakondaiah, G. Vaitheeswaran, and S. Lebègue, "Structural, vibrational, and quasiparticle band structure of 1,1-diamino-2,2-dinitroethelene from *ab initio* calculations," J. Chem. Phys. **140**, 014105 (2014).

[33] S. Appalakondaiah, G. Vaitheeswaran, and S. Lebègue, "Dispersion corrected structural properties and quasiparticle band gaps of several organic energetic solids," J. Phys. Chem. A **119**, 6574 (2015).

[34] M. R. Baer, "Modeling heterogeneous energetic materials at the mesoscale," Thermochim. Acta **384**, 351 (2002).

[35] H. R. James and B. D. Lambourn, "On the systematics of particle velocity histories in the shock-to-detonation transition regime," J. Appl. Phys. **100**, 084906 (2006).

[36] A. Keyhani and M. Zhou, "Thermo-mechanical response of an additively manufactured energetic material simulant to dynamic loading," J. Dyn. Behav. Mater. **6**, 502 (2020).

[37] D. E. Kittell, C. D. Yarrington, M. L. Hobbs, M. J. Abere, and D. P. Adams, "A diffusion-limited reaction model for self-propagating Al/Pt multilayers with quench limits," J. Appl. Phys. **123**, 145302 (2018).

[38] R. N. Mulford and D. C. Swift, "'Mesoscale modelling of shock initiation in HMX-based explosives," AIP Conf. Proc. **620**, 415 (2002).

[39] B. Nili, G. Subhash, and J. S. Tulenko, "Coupled electro-thermo-mechanical simulation for multiple pellet fabrication using spark plasma sintering," J. Manuf. Sci. Eng. **140**, 051010 (2018).

[40] J. J. Rimoli, E. Gürses, and M. Ortiz, "Shock-induced subgrain microstructures as possible homogenous sources of hot spots and initiation sites in energetic polycrystals," Phys. Rev. B **81**, 014112 (2010).

[41] U. Roy, S. Kim, C. Miller, Y. Horie, and M. Zhou, "Computational study of ignition behavior and hotspot dynamics of a potential class of aluminized explosives," Modell. Simul. Mater. Sci. Eng. **26**, 085004 (2018).

[42] K. B. Wagner, A. Keyhani, A. K. Boddorff, G. Kennedy, D. Montaigne, B. J. Jensen, M. Beason, M. Zhou, and N. N. Thadhani, "High-speed x-ray phase contrast imaging and digital image correlation analysis of microscale shock response of an additively manufactured energetic material simulant," J. Appl. Phys. **127**, 235902 (2020).

[43] E. J. Welle, C. D. Molek, R. R. Wixom, and P. Samuels, "Microstructural effects on the ignition behavior of HMX," (IOP Publishing), J. Phys.: Conf. Ser. **500**, 052049 (2014).

[44] R. R. Wixom, A. S. Tappan, A. L. Brundage, R. Knepper, M. B. Ritchey, J. R. Michael, and M. J. Rye, "Characterization of pore morphology in molecular crystal explosives by focused ion-beam nanotomography," J. Mater. Res. **25**, 1362 (2010).

[45] C. Yarrington, R. R. Wixom, and D. L. Damm, *Mesoscale Simulations Using Realistic Microstructure and First Principles Equation of State* (Sandia National Lab, Albuquerque, NM, 2012).

[46] N. Yedukondalu and G. Vaitheeswaran, "Polymorphism, phase transition, and lattice dynamics of energetic oxidizer ammonium perchlorate under high pressure," J. Phys. Chem. C **123**, 2114 (2019).

[47] M. M. Kuklja, R. Tsyshevsky, A. S. Zverev, A. Mitrofanov, N. Ilyakova, D. R. Nurmukhametov, and S. N. Rashkeev, "Achieving tunable chemical reactivity through photo-initiation of energetic materials at metal oxide surfaces," Phys. Chem. Chem. Phys. **22**, 25284 (2020).

[48] X. Ma, K. Cao, X. Huang, S. Yang, Y. Ye, R. Shen, G. Yang, and K. Zhang, "*In situ* synthesized MEMS compatible energetic arrays based on energetic coordination polymer and nano-Al with tunable properties," ACS Appl. Mater. Interfaces **12**, 30740 (2020).

[49] J. H. Shin and M. Zhou, "Piezoelectric response of energetic composites under an electrostatic excitation," J. Appl. Phys. **129**, 245103 (2021).

[50] S. Jain, S. Chakraborty, and L. Qiao, "Burn rate enhancement of ammonium perchlorate–nitrocellulose composite solid propellant using copper oxide–graphene foam micro-structures," Combust. Flame **206**, 282 (2019).

[51] M. Örnek, K. E. Uhlenhake, Y. Zhou, B. Zhang, M. Kalaswad, D. N. Collard, H. Wang, Q. Wang, and S. F. Son, "Preparation and characterization of multi-functional piezoenergetic polyvinylidene fluoride/aluminum nanocomposite films," J. Appl. Phys. **131**, 055108 (2022).

[52] J. H. Shin, D. K. Messer, M. Örnek, S. F. Son, and M. Zhou, "Dielectric breakdown driven by flexoelectric and piezoelectric charge generation as hotspot ignition mechanism in aluminized fluoropolymer films," J. Appl. Phys. **132**, 085101 (2022).

[53] D. K. Messer, J. H. Shin, M. Örnek, T. A. Hafner, M. Zhou, and S. F. Son, "Effects of flexoelectric and piezoelectric properties on the impact-driven ignition sensitivity of P(VDF-TrFE)/nAl films," Combust. Flame **242**, 112181 (2022).

[54] J. B. DeLisio, X. Hu, T. Wu, G. C. Egan, G. Young, and M. R. Zachariah, "Probing the reaction mechanism of aluminum/poly(vinylidene fluoride) composites," J. Phys. Chem. B **120**, 5534 (2016).

[55] R. S. Janesheski, L. J. Groven, and S. F. Son, "'Fluoropolymer and aluminum piezoelectric reactivities," AIP Conf. Proc. **1426**, 741 (2012).

[56] J. McCollum, A. M. Morey, and S. T. Iacono, "Morphological and combustion study of interface effects in aluminum-poly(vinylidene fluoride) composites," Mater. Des. **134**, 64 (2017).

[57] J. McCollum, M. L. Pantoya, and S. T. Iacono, "Activating aluminum reactivity with fluoropolymer coatings for improved energetic composite combustion," ACS Appl. Mater. Interfaces **7**, 18742 (2015).

[58] T. R. Sippel, S. F. Son, and L. J. Groven, "Altering reactivity of aluminum with selective inclusion of polytetrafluoroethylene through mechanical activation," Propellants, Explos., Pyrotech. **38**, 286 (2013).

[59] T. R. Sippel, S. F. Son, and L. J. Groven, "Aluminum agglomeration reduction in a composite propellant using tailored Al/PTFE particles," Combust. Flame **161**, 311 (2014).

[60] S. K. Valluri, M. Schoenitz, and E. Dreizin, "Fluorine-containing oxidizers for metal fuels in energetic formulations," Def. Technol. **15**, 1 (2019).

[61] H. Wang, M. Rehwoldt, D. J. Kline, T. Wu, P. Wang, and M. R. Zachariah, "Comparison study of the ignition and combustion characteristics of directly-written Al/PVDF, Al/Viton and Al/THV composites," Combust. Flame **201**, 181 (2019).

[62] K. J. Laidler, "The development of the Arrhenius equation," J. Chem. Educ. **61**, 494 (1984).

[63] J. T. Mang, R. P. Hjelm, S. F. Son, P. D. Peterson, and B. S. Jorgensen, "Characterization of components of nano-energetics by small-angle scattering techniques," J. Mater. Res. **22**, 1907 (2007).

[64] Y. Li and M. Zhou, "Effect of competing mechanisms on fracture toughness of metals with ductile grain structures," Eng. Fract. Mech. **205**, 14 (2019).

14 March 2024 04:23:33

[65]Y. Li and M. Zhou, "Prediction of fracture toughness of ceramic composites as function of microstructure: I.: Numerical simulations," J. Mech. Phys. Solids **61**, 472 (2013).

[66]Y. Li and M. Zhou, "Prediction of fracture toughness of ceramic composites as function of microstructure: II. Analytical model," J. Mech. Phys. Solids **61**, 489 (2013).

[67]C. Miller, D. Kittell, C. Yarrington, and M. Zhou, "Prediction of probabilistic detonation threshold via millimeter-scale microstructure-explicit and void-explicit simulations," Propellants, Explos., Pyrotech. **45**, 254 (2020).

[68]A. Barua, S. P. Kim, Y. Horie, and M. Zhou, "'Computational analysis of ignition in heterogeneous energetic materials,' (Trans Tech Publ)," Mater. Sci. Forum **767**, 13 (2014).

[69]U. Roy and M. Zhou, "A computational framework for predicting the fracture toughness of metals as function of microstructure," J. Mech. Phys. Solids **142**, 103955 (2020).

[70]U. Roy, D. L. McDowell, and M. Zhou, "Effect of grain orientations on fracture behavior of polycrystalline metals," J. Mech. Phys. Solids **151**, 104384 (2021).

[71]J. H. Shin, D. Olsen, C. Coffelt, L. S. Martin, and M. Zhou, "Dielectric breakdown of heterogeneous materials under electromagnetic pulses," J. Mater. Res. **37**, 4059 (2022).

[72]J. H. Shin, M. J. Zaitzeff, L. J. Groven, and M. Zhou, "Microstructural effects on microscopic and homogenized macroscopic flexoelectric behavior of THV/Al composites," J. Appl. Phys. **133**, 164101 (2022).

[73]W. N. Dos Santos, C. Y. Iguchi, and R. Gregorio Jr, "Thermal properties of poly(vinilidene fluoride) in the temperature range from 25 to 210 C," Polym. Test. **27**, 204 (2008).

[74]P. Foteinopoulos, A. Papacharalampopoulos, and P. Stavropoulos, "On thermal modeling of additive manufacturing processes," CIRP J. Manuf. Sci. Technol. **20**, 66 (2018).

[75]D. S. Sundaram, P. Puri, and V. Yang, "A general theory of ignition and combustion of nano-and micron-sized aluminum particles," Combust. Flame **169**, 94 (2016).

[76]A. Barua, S. Kim, Y. Horie, and M. Zhou, "Ignition criterion for heterogeneous energetic materials based on hotspot size-temperature threshold," J. Appl. Phys. **113**, 064906 (2013).

[77]S. Zeman and M. Jungová, "Sensitivity and performance of energetic materials," Propellants, Explos., Pyrotech. **41**, 426 (2016).

[78]G. F. Adams and R. W. Shaw Jr, "Chemical reactions in energetic materials," Annu. Rev. Phys. Chem. **43**, 311 (1992).

[79]A. F. Belyaev, Y. V. Frolov, and A. I. Korotkov, "Combustion and ignition of particles of finely dispersed aluminum," Combust., Explos. Shock Waves **4**, 182 (1968).

[80]C. Weir, M. L. Pantoya, and M. A. Daniels, "The role of aluminum particle size in electrostatic ignition sensitivity of composite energetic materials," Combust. Flame **160**, 2279 (2013).

[81]Z. Yu'nan, L. Jianzhong, D. Liang, S. Wei, Y. Weijuan, and Z. Junhu, "Effect of particle size and oxygen content on ignition and combustion of aluminum particles," Chin. J. Aeronaut. **30**, 1835 (2017).

[82]L. Q. Xiao, X. Z. Fan, J. Z. Li, Z. Qin, X. L. Fu, W. Q. Pang, and Y. Wang, "Effect of Al content and particle size on the combustion of HMX-CMDB propellant," Combust. Flame **214**, 80 (2020).

[83]C. Miller, D. Olsen, Y. Wei, and M. Zhou, "Three-dimensional microstructure-explicit and void-explicit mesoscale simulations of detonation of HMX at millimeter sample size scale," J. Appl. Phys. **127**, 125105 (2020).

14 March 2024 04:23:33